SLOTTED GROUND STRUCTURES AND THEIR APPLICATIONS TO VARIOUS MICROWAVE COMPONENTS

A Thesis

by

DONG JIN JUNG

Submitted to the Office of Graduate Studies of
Texas A&M University
in partial fulfillment of the requirements for the degree of

MASTER OF SCIENCE

May 2009

Major Subject: Electrical Engineering

SLOTTED GROUND STRUCTURES AND THEIR APPLICATIONS TO VARIOUS MICROWAVE COMPONENTS

A Thesis

by

DONG JIN JUNG

Submitted to the Office of Graduate Studies of
Texas A&M University
in partial fulfillment of the requirements for the degree of

MASTER OF SCIENCE

Approved by:

Chair of Committee,	Kai Chang
Committee Members,	Gregory H. Huff
	Laszlo B. Kish
	Hae-Kwon Jeong
Head of Department,	Costas N. Georghiades

May 2009

Major Subject: Electrical Engineering

ABSTRACT

Slotted Ground Structures and Their Applications to Various Microwave Components. (May 2009)

Dong Jin Jung, B.S., Soonchunhyang University, Korea

Chair of Advisory Committee: Dr. Kai Chang

This thesis discusses microstrip circuits and components with a slotted area on the ground plane. In recent years, various slot geometries have been placed on the ground plane with the purpose of reducing harmonics, producing frequency pass/stop-bands, and enhancing coupling effects. Among several ground slot geometries, a dumbbell shaped slot (DSS) is attractive because of its simple structure and easy analysis. The DSS and its applications to RF/microwave filters are studied and discussed. A lumped equivalent circuit model of the dumbbell shaped ground slot is introduced by utilizing resonator and filter theories. The accuracy of the equivalent circuit model is demonstrated through the comparison of circuit simulations and measurements. A lowpass filter (LPF) using slotted ground structure (SGS) with dumbbell shape is designed and measured to validate its theories. By using SGS techniques presented in this thesis, some other RF/microwave components such as a periodic structure, ultra-wideband bandpass filter (UWB-BPF), and rectenna with SGS-LPF are designed and tested.

DEDICATION

This thesis is dedicated to my parents.

ACKNOWLEDGEMENTS

I would like to express my deepest gratitude to my advisor Dr. Kai Chang for his guidance and support with regards to my graduate studies and research at Texas A&M. My appreciation goes out to Dr. Gregory H. Huff, Dr. Laszlo B. Kish, and Dr. Hae-Kwon Jeong for serving as committee members for my thesis. I would also like to thank Mr. Li at Texas A&M University for their helpful support in the development of the projects described in this thesis. I also want to express my gratitude to my former advisors, Dr. Dal Ahn and Dr. Jong-Sik Lim, for their support and dedication with regards to my undergraduate studies. Especially, Dr. Dal Ahn has always encouraged me to have positive thoughts and guided me with helpful suggestions. Thanks also go to all my friends and EML (Electromagnetic and Microwave Laboratory) colleagues, Chi-Hyung, Sung-Won, Jung-Kyu, Chan-Ho, David, Yachi, Travis, Sean, Andrew, Jacob, and Vipin.

Special thanks go to my parents, Mrs. Youn-Soon Ahn and Mr. Hoon-Mo Jung, for their encouragement and love. I also express my thanks to my younger brother, Jin-Hyuck.

Finally, I thank my God for his guidance and help.

NOMENCLATURE

DSS	Dumbbell Shaped Slot
LPF	Low-pass Filter
SGS	Slotted Ground Structure
UWB	Ultra-wide Band
BPF	Band-pass Filter
EBG	Electromagnetic Band-gap
PC's	Photonic Crystals
PBG	Photonic Band-gap
EM	Electromagnetic
DGS	Defected Ground Structure
DS	Dumbbell Shaped
PEC	Perfect Electric Conductor
PMC	Perfect Magnetic Conductor
TEM	Transverse Electromagnetic
FCC	Federal Communications Commission
CPW	Coplanar Waveguide
FEM	Finite Element Method
MMIC	Microwave Monolithic Integrated Circuit
VSWR	Voltage Standing Wave Ratio
MOM	Method of Momentum

TABLE OF CONTENTS

CHAPTER Page

LIST OF FIGURES

FIGURE Page

FIGURE Page

FIGURE Page

LIST OF TABLES

CHAPTER I

INTRODUCTION

Electromagnetic band-gap (EBG) materials known as photonic crystals (PC's) or photonic band-gap (PBG) are a new class of artificially fabricated structures which have the ability to control the propagation of electromagnetic (EM) waves [1]. Recently, various RF and microwave components with slots in the ground plane have been reported [2]-[7]. These structures, known as defected ground structures (DGS), may be treated as electromagnetic band-gap (EBG) structures since they allow or forbid wave propagation at certain frequency bands. Any periodic structure or slot geometry on the ground plane can disturb the field distribution of the guided electromagnetic wave and create an EBG effect in some frequency ranges. This EBG effect is useful for suppressing harmonics and preventing undesired signals in components, the primary function of filters. As the frequency spectrum becomes increasingly crowded, an accurate filter design is necessary for system performance and interference prevention. Various slotted geometries on ground plane have been reported and found [8]-[10]. These slotted ground structures (SGS) are realized by etching off certain geometry from the conducting ground plane. Among several slot geometries, a dumbbell shaped-slotted ground structure (DS-SGS) has attracted many researchers' attention because of its simple structure and easy analysis method.

This thesis follows the style of *IEEE Transactions on Microwave Theory and Techniques*.

The lumped equivalent circuit model of this dumbbell shaped slot (DSS) has been reported in [11]. Basically, a simulated frequency response of a DSS shows the band-gap (or band-stop) characteristic. This simulated frequency response is used to extract the equivalent circuit components of a DSS. In this thesis, a simple slotted ground structure with a dumbbell shape is extensively studied to extract its lumped equivalent circuit model and mathematical expressions. In order to suggest an accurate equivalent circuit model of the dumbbell shaped slot, a loss analysis from this slot section is performed. Through these investigations, modified mathematical expressions for DSS are proposed and used for lowpass filter (LPF) design that doesn't produce a cutoff frequency error. Ultra-wide band (UWB) band-pass design using two simple rectangle ground slots is also introduced.

By placing the dumbbell shaped slot underneath the microstrip transmission line, the anti-resonant frequency response is observed. This dumbbell shaped slot in the ground plane disturbs the guided field distributions and the disturbance changes the characteristics of inductance and capacitance of the transmission line. Thus, the propagation constant of the transmission line is changed. Periodic structures with dumbbell shaped slots are also studied from this theory.

For the theoretical background, this thesis begins with a low-pass filter design of insertion loss method because this filter synthesis method is useful for analyzing a DSS in the ground. Because the EM simulated S-parameter characteristics of a single DSS show a similar frequency response to a Butterworth (or maximally flat) prototype LPF (N=1) [12], which is one of the insertion loss methods, a DSS can be analyzed by the

general LPF design theory. To validate all the theories in this thesis, simulation and measured results are provided. Good agreement between the theory and experiments has been achieved.

CHAPTER II

BACKGROUND

A. Insertion Loss Method

A filter that allows or forbids the certain frequency range is an important component in RF/microwave systems. High performance, compact size, and low production cost are required for modern microwave filters. The filter design with SGS can meet these requirements through its several advantages such as compact size, simple design process, and suppressing higher harmonics.

In this section, the insertion loss method which is one of the general filter design theories is presented for practical design with SGS. For modern microwave filters, the insertion loss method is more desirable as compared to the image parameter method. In the insertion loss method, a pass-band ripple and attenuation characteristics are accurately predicted, but they can not be predicted in the image parameter method. In the insertion loss method a filter response is defined by its insertion loss or *power loss ratio* in (1).

$$P_{LR} = \frac{\text{Power availible from source}}{\text{Power delivered to load}} = \frac{P_{incident}}{P_{load}} = \frac{1}{1-\left|\Gamma\left(\omega\right)\right|^2} \tag{1}$$

Since $|\Gamma(\omega)|^2$ is an even function in terms of ω from (1), it can be expressed as a polynomial of ω^2 in (2).

$$\left|\Gamma\left(\omega\right)\right|^2 = \frac{M\left(\omega^2\right)}{M\left(\omega^2\right)+N\left(\omega^2\right)} \tag{2}$$

By substituting (2) into (1), the following is obtained:

$$P_{LR} = 1 + \frac{M\left(\omega^2\right)}{N\left(\omega^2\right)} \tag{3}$$

This equation specifies that the power loss ratio in the insertion loss method has the form of (3). Equations (1)-(3) are found in [13].

There are three different attenuation characteristics in the insertion loss methods: *maximally fla*t (or *Butterworth*), *equal ripple* (or *Chebyshev*), and *elliptic function*. Only the maximally flat deign theory is introduced. The following maximally flat filter theory can be found [14].

B. Maximally Flat Lowpass Filter

This type of filters provides the flat pass-band with a smooth cutoff characteristic. Its attenuation characteristic is shown in Fig. 1. Equation (4) shows a mathematical expression of maximally flat attenuation characteristic. In (4), ω' represents a variable for prototype frequencies. ε is determined in (5), where L_{Ar} is defined as 3 dB.

$$L_A\left(\omega'\right) = 10\log_{10}\left[1 + \varepsilon\left(\frac{\omega'}{\omega_1'}\right)^{2n}\right] \quad \text{[dB]} \tag{4}$$

$$\varepsilon = \left[anti\log_{10}\frac{L_{Ar}}{10}\right] - 1 \tag{5}$$

When the attenuation ($L_A(\omega')$) is 3 dB, the frequency (ω_1') in (4) is defined as the pass-band edge (or prototype 3 dB cutoff frequency). ε is approximately calculated as 0.995262 when $\omega' = \omega_1'$ (L_A=L_{Ar}).

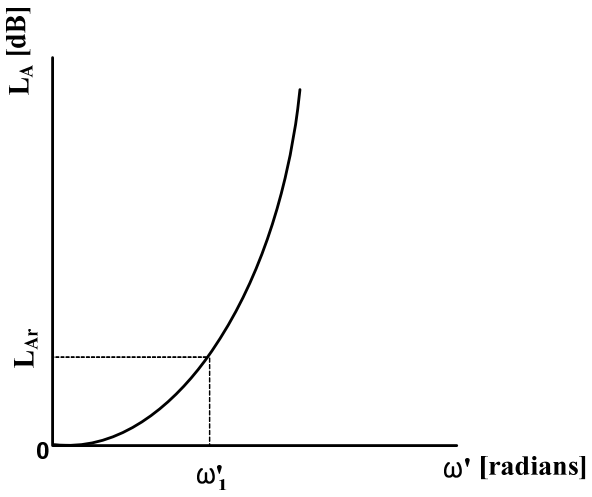

Fig. 1. A maximally flat low-pass attenuation characteristic.

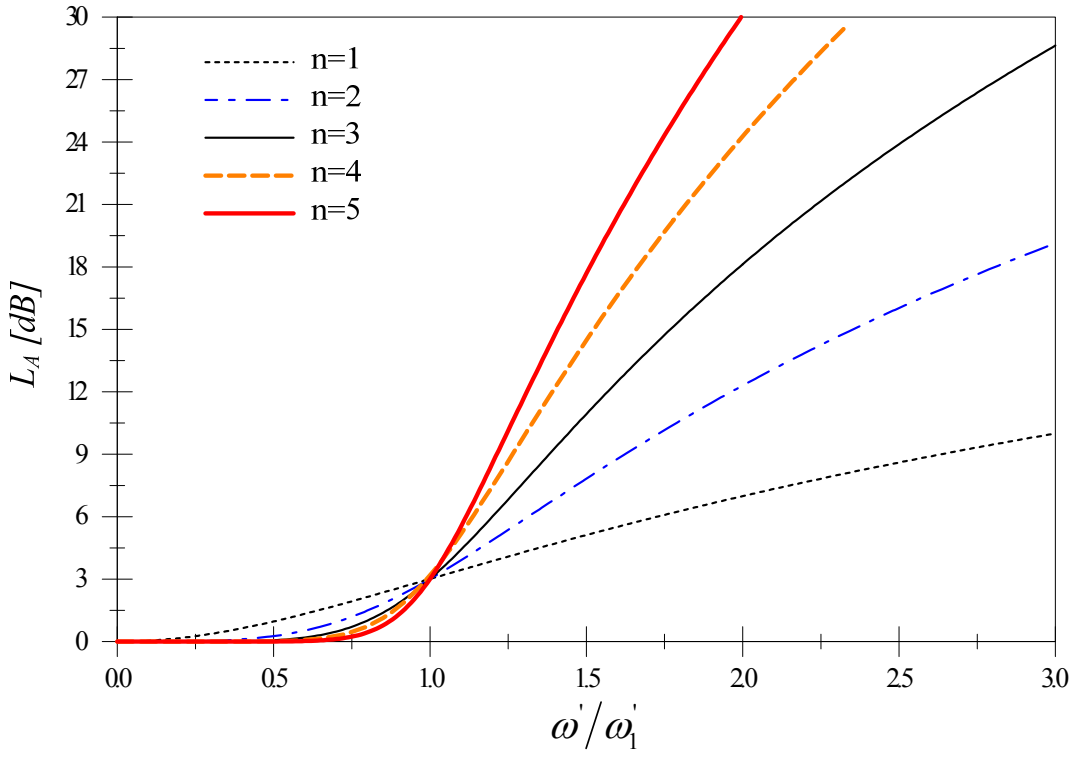

Fig. 2. The maximally flat type attenuation characteristics depending on the number of reactive elements.

The response in Fig. 2 can be achieved by the prototype low-pass filter circuits shown in Fig. 3.

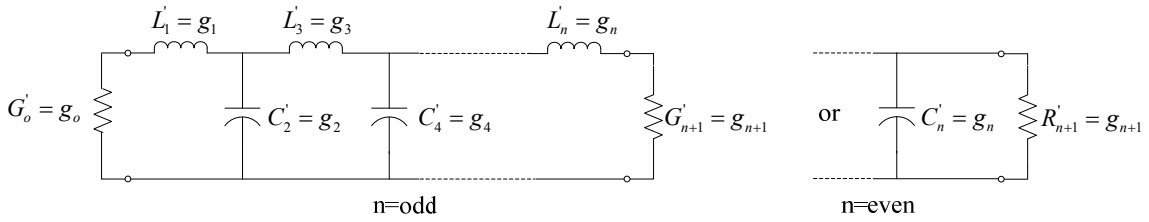

(a)

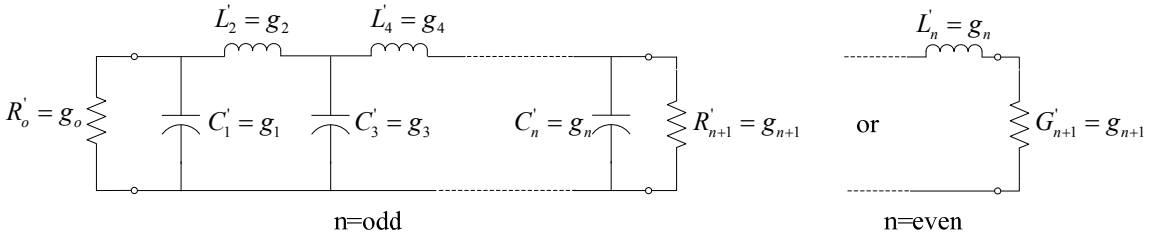

(b)

Fig.3. Definition of the prototype low-pass filters (a) *T*-type and its dual, (b) π-type.

In Fig. 3, the following conventions are observed:

$$g_k\big|_{k=1 \text{ to n}} = \begin{Bmatrix} \text{The inductance of a series element} \\ \text{The capacitance of a shunt element} \end{Bmatrix}$$

$$g_o = \begin{Bmatrix} \text{The source is resistance if } g_1 = C_1' \\ \text{The source is conductance if } g_1 = L_1' \end{Bmatrix}$$

$$g_{n+1} = \begin{Bmatrix} \text{The load is resistance if } g_n = C_n' \\ \text{The load is conductance if } g_n = L_n' \end{Bmatrix}$$

Prototype parameters of the maximally flat prototype filters can be computed by (6) and (7) [15].

$$g_o = g_{n+1} = 1 \tag{6}$$

$$g_k = 2\sin\left[\frac{(2k-1)\pi}{2n}\right] \ , k = 1, 2, 3, \cdots, n \tag{7}$$

Table 1 shows the prototype element values for filters with the maximally flat attenuation characteristic. Since the prototype element values determined in (6) and (7) are all normalized to make $g_0 = 1$ and $\omega_1' = 1$, the impedance and frequency transformation are required for its actual element values.

Table 1. Prototype element values for filters with maximally flat attenuation

n	g_1	g_2	g_3	g_4	g_5	g_6	g_7	g_8
1	2.0000	1.0000						
2	1.4140	1.4140	1.0000					
3	1.0000	2.0000	1.0000	1.0000				
4	0.7654	1.8480	1.8480	0.7654	1.0000			
5	0.6180	1.6180	2.0000	1.6180	0.6180	1.0000		
6	0.5176	1.4140	1.9320	1.9320	1.4140	0.5176	1.0000	
7	0.4450	1.2470	1.8020	1.8020	1.8020	1.2470	0.4450	1.0000

Once a set of normalized prototype element values have been selected, the next step is to convert the prototype values into real scale values in order to design a filter that has the cutoff frequency and impedance level of the given design specifications. This process is called as scaling or de-normalization of the prototype values. The frequency

transformation and impedance scaling are used in the process and they are discussed in the following sections.

C. Frequency Transformation

The frequency transformation function from a prototype frequency to real frequency can be found in Fig. 4.

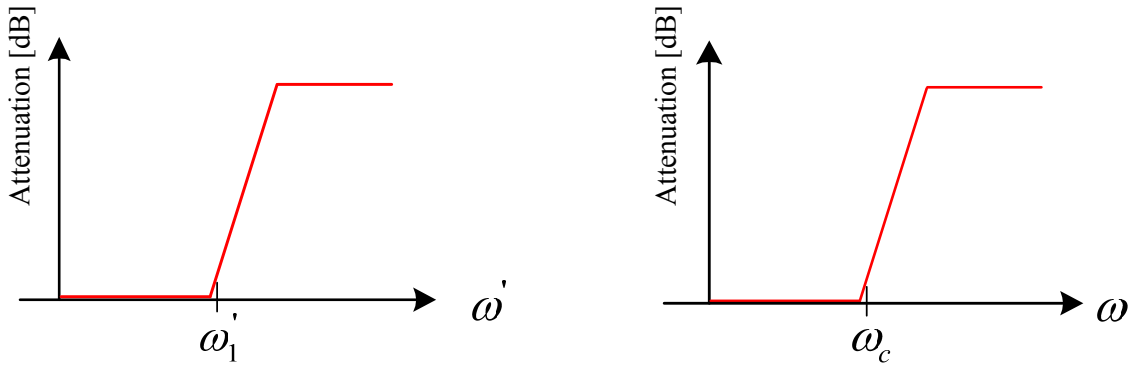

(a) (b)

Fig. 4. Low-pass filter attenuation characteristics in (a) prototype frequency domain and (b) real frequency domain.

The transformation function can be obtained from the proportional expression of Fig. 4. Equation (8) holds (9).

$$\omega_1' : \omega' = \omega_c : \omega \tag{8}$$

$$\omega' = \frac{\omega_1'}{\omega_c}\omega \tag{9}$$

In Fig. 3 (a), the first series inductor and second parallel capacitor can be expressed as an impedance form in (10).

$$\begin{aligned} &\text{The series inductor : } jg_1\omega' \\ &\text{The parallel capacitor : } \frac{1}{j\omega' g_2} \end{aligned} \tag{10}$$

By substituting the frequency transformation function (9) into (10), the impedance of the series inductor and parallel capacitor are shown in (11).

$$\begin{aligned} &\text{The series inductor : } j\omega\left(\frac{\omega_1' g_1}{\omega_c}\right) = j\omega L_1 \\ &\text{The parallel capacitor : } \frac{1}{j\omega\left(\frac{\omega_1' g_2}{\omega_c}\right)} = \frac{1}{j\omega C_2} \end{aligned} \tag{11}$$

As mentioned above, the prototype cutoff frequency is defined as $\omega_1' = 1$, so the first series inductor and second parallel capacitor in the real frequency domain can be expressed in the form of (12).

$$\begin{aligned} L_1 &= \frac{g_1}{\omega_c} \\ C_2 &= \frac{g_2}{\omega_c} \end{aligned} \tag{12}$$

D. Impedance Scaling

If n has the odd number of elements in Fig. 3 (b), the source and load terminations have the resistance. These resistances are unity in the prototype design because the source and load terminations are normalized by the original terminating resistance. In case of that the termination has the conductance, the termination is scaled by the original terminating conductance. When the original source and load terminating resistance is R_0, the impedance scaling of the series inductance and parallel capacitance in (12) can be shown in (13).

$$\begin{aligned} L_1 &= \frac{g_1 \cdot R_o}{\omega_c} \\ C_2 &= \frac{g_2}{R_o \cdot \omega_c} \end{aligned} \tag{13}$$

Finally, the general expressions of the frequency and impedance scaling for a prototype low-pass filter have the form of (14)

$$\begin{aligned} L_k &= \frac{g_k \cdot R_o}{\omega_c} \\ C_k &= \frac{g_k}{R_o \cdot \omega_c} \ , k = 1, 2, 3, \cdots, n \end{aligned} \tag{14}$$

CHAPTER III

THEORY OF DUMBBELL SHAPED SLOT

A. Modeling Equivalent Circuit of DSS

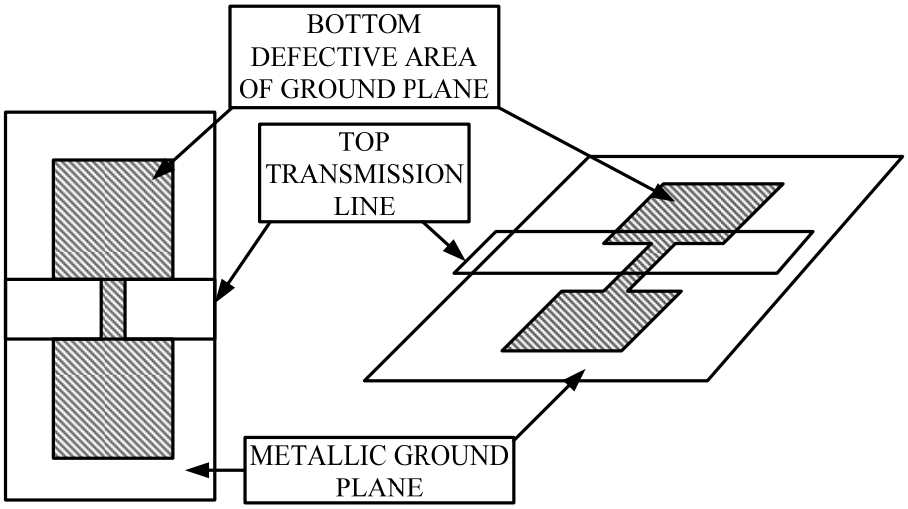

Fig. 5. Microstrip transmission line with a single DSS on the ground plane.

As mentioned above, this thesis treats a DSS on the ground plane as a parallel *LC* resonator due to its band-stop frequency response characteristic. EM simulation of a DSS structure is required because the 3 dB cutoff and anti-resonant frequency of the DSS are the key information to find the equivalent inductance and capacitance. Once that frequency information is found, the equivalent inductance and capacitance of the DSS can be calculated by the general insertion loss method LPF design equation and a resonator theory. Figure 5 shows the microstrip configurations consisting of a 50 ohm transmission line and a single DSS underneath the microstrip line.

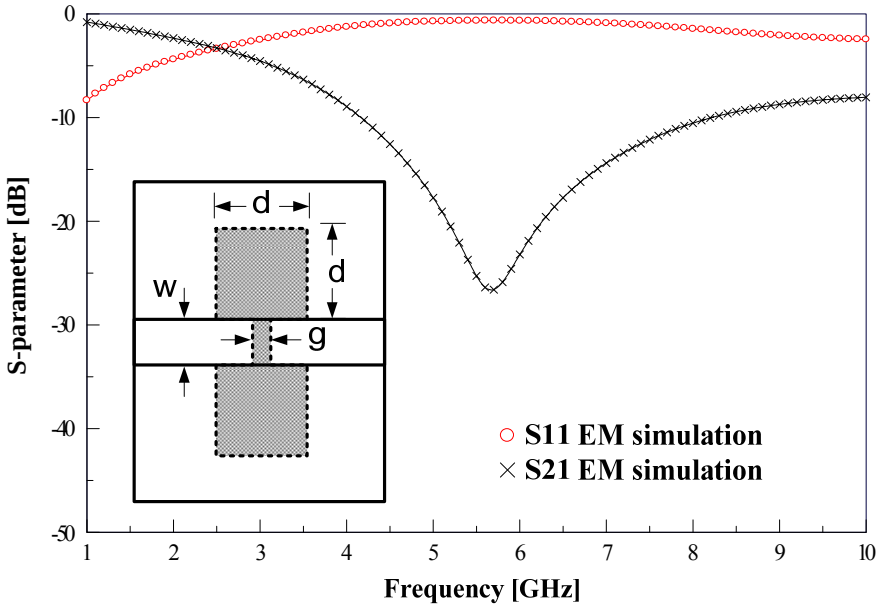

Fig. 6. EM simulation of microstrip line with the DSS dimensions of d=7.5 mm, g=0.3 mm, and w=2.3 mm (substrate thickness=30 mil and ε_r =2.2).

In Fig. 6, EM simulation of the single DSS shows a 3dB cutoff frequency of 2.5 GHz and an anti-resonant frequency of 5.7 GHz. There is only one anti-resonant pole at 5.7 GHz, which means that the inductance and capacitance due to the DSS dimensions are unique over the frequencies. In the frequency bands from 1.0 GHz to 5.7 GHz, the DSS shows similar S-parameter characteristics as a maximally flat type LPF (N=1) designed to have the same cutoff frequency of 2.5 GHz. Thus, a parallel LC resonator which is the equivalent circuit of a single DSS can be equated with the maximally flat type LPF with N=1 and f_c=2.5 GHz.

Figure 7 shows a lumped equivalent circuit model of a maximally flat prototype LPF (N=1) and a single DSS in the ground plane. Equations (15) and (16) can be found from Fig.7 and (14).

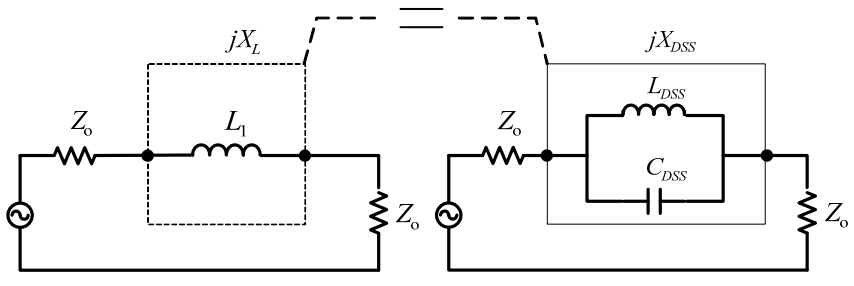

(a) (b)

Fig. 7. Equivalent circuit models of (a) a prototype LPF (N=1) and (b) a single DSS.

$$jX_L = j \cdot \omega L_1 = j \cdot \omega \frac{g_1 Z_o}{\omega_c} \tag{15}$$

where g_1=2.

$$jX_{DSS} = j \cdot \frac{1}{\omega_r C_{DSS} \left(\omega_r / \omega - \omega / \omega_r \right)} \tag{16}$$

Since (15) and (16) have the same reactance at $\omega=\omega_c$, the following holds:

$$jX_L = jX_{DSS} \tag{17}$$

Equation (17) results in (18), which gives the equivalent capacitance. Once the capacitance is found, the other equivalent circuit component, inductance can be easily calculated from (19).

$$C_{DSS} = \frac{1}{g_1 \cdot Z_o \cdot \omega_r \left(\omega_r / \omega_c - \omega_c / \omega_r \right)} \tag{18}$$

$$L_{DSS} = \frac{1}{\omega_r^2 \cdot C_{DSS}} \tag{19}$$

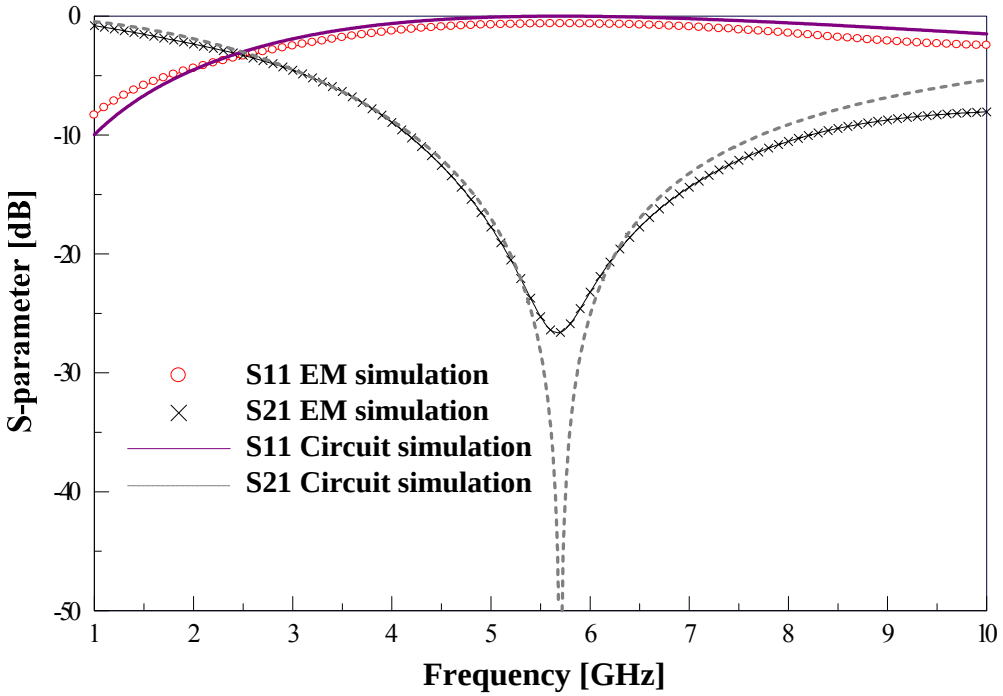

Fig. 8. EM and circuit simulations from the conventional equivalent circuit extracting method for a single DSS with the dimensions of d=7.5 mm and g=0.3 mm (L_{DSS}=5.163 nH and C_{DSS}=0.151 pF).

Based on the above analysis, the equivalent inductance and capacitance of a single DSS with the dimensions of d=7.5 mm and g=0.3 mm are 5.163 nH and 0.151 pF, respectively. With these calculated circuit components, EM and circuit simulation results are compared in Fig. 8. As shown in Fig. 8, the equivalent circuit components of a DSS can be easily found. In spite of the simple calculation for an equivalent circuit, a LPF design with a DSS is limited by finding the proper DSS dimensions to meet the required specifications. In filter design the filter dimensions should be defined from the given design specifications (the cutoff frequency, pass and stop-band, the number of element

stages, and etc.). In other words, designing a filter should start from the design specifications. In LPF design with a DSS, the cutoff frequency of the DSS dimensions must be equal to the specified design cutoff frequency. This means that one cannot design a LPF with a DSS if the DSS dimensions producing the same cutoff frequency are not found. As a result, the curve fitting analysis is required to find the DSS dimensions from the calculated equivalent inductance and capacitance.

B. Modeling Losses of DSS

As shown in Fig. 8, the anti-resonant peak points of the circuit and EM simulations are different. The difference of these peak points is caused due to losses of the microstrip transmission line and a loss of slotted ground section. In practical case, microstrip transmission line has the dielectric, conductor, and radiation losses. The conductor loss caused by the finite conductivity of the conducting microstrip line and ground plane is represented by the series resistance, and the dielectric loss caused by the complex permittivity of dielectric material is represented by the shunt conductance [16]. Normally, a radiation loss is generated due to the impedance mismatching and discontinuity of a transmission line.

In order to consider a loss of the slotted ground discontinuity through EM simulation, microstrip line and ground plane are selected with a perfect electric conductor (PEC), i.e., no conductor loss. A very small dielectric loss, which can be disregard, is assumed since a low loss dielectric material is used for a microstrip. Radiation loss can be also disregard at anti-resonance because the return loss is 0 dB in

Fig. 8, which means that almost all incident power is reflected back to the input port at resonance. This can be regarded as mismatch loss at anti-resonance, thus the incident power is reflected back to input. The mismatch between the source impedance (50 ohm) and input impedance of a slotted ground section is occurred since the slot area on the ground changes the characteristic capacitance and inductance of a transmission line. By changing these characteristic capacitance and impedance of the transmission line, the characteristic impedance of transmission line with slotted ground section is also changed by (20).

$$Z_c = \sqrt{\frac{L}{C}} = \sqrt{\frac{\mu_0 \varepsilon_0}{C C_a}} = \sqrt{\frac{L}{C_a}} \sqrt{\frac{C_a}{C}} = \frac{Z_{co}}{\sqrt{\varepsilon_e}} \tag{20}$$

In (20), Z_{c0} and C_a is the characteristic impedance and capacitance of the air-filled line and the ratio C/C_a gives the effective dielectric constant ε_e [17]. For these reasons anti-resonant peak point of EM simulation in Fig. 8, which is near 27dB, is mostly related with the mismatch loss between the source impedance and input impedance of the dumbbell shaped-slotted ground section at anti-resonance. Thus, if the equivalent circuit simulation of the dumbbell shaped-slotted ground section, which includes a radiation and mismatch loss, matches the measured data, it proves that this circuit model presents the exact equivalent circuit of the slotted ground section.

In order to model the loss of a slotted ground structure as a circuit parameter, DSS with different slot dimensions are used to confirm the reliability of the previous theory. A new DSS dimensions with d=5 mm and g= 0.7 mm are fabricated on substrate with h=30 mil and ε=2.2. From the previous theory, C_{DSS} and L_{DSS} are found as 0.096 pF

and 3.4072 nH, respectively. Figure 9 shows the simulated and measured results with the dimensions of d= 5 mm and g=0.7 mm. As it is shown, the anti-resonant point of the simulated result does not match the one of measured. The magnitude of the measured S_{21} resonant point is 27 dB in Fig. 9.

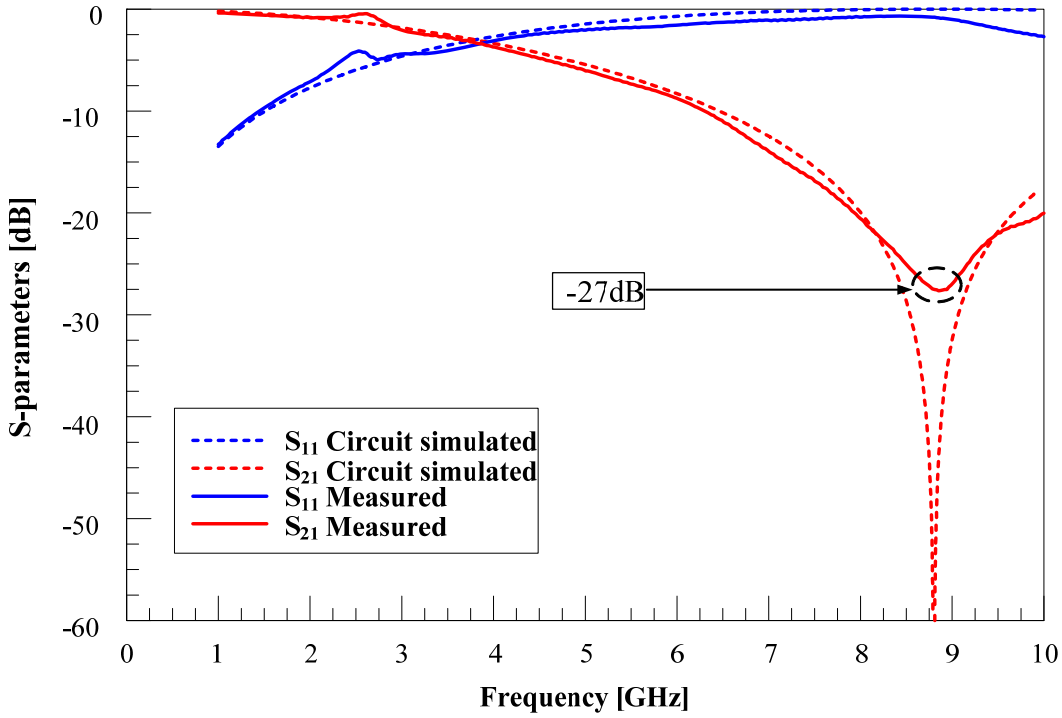

Fig. 9. Circuit simulation and measured s-parameters of a DSS with the dimensions of d=5 mm and g=0.7 mm.

To present the radiation and mismatch loss, the resistance (R_{DSS}) is added to a LC parallel resonator which is the equivalent circuit model of the slotted ground section in lossless case. Figure 10 (a) shows the complete equivalent circuit model of the slotted ground section. The impedance of DSS section in the ground can be expressed as (21).

$$Z_{DSS} = \frac{1}{Y_{DSS}} = \frac{1}{\frac{1}{R_{DSS}} + j\left(\omega C_{DSS} - \frac{1}{\omega L_{DSS}}\right)} \tag{21}$$

At resonance the imaginary part of (21) is zero. Equation (21) can be expressed as (22) at its resonance.

$$Z_{DSS} = R_{DSS} \quad \text{at } \omega=\omega_o \tag{22}$$

The series resistance R_{DSS} representing the radiation and mismatch loss can be determined through measured or EM simulated S_{21}. The following steps from (23) to (27) show the mathematical derivation for the series resistance, $R_{DSS.}$ *ABCD* matrix can be set to (23) from Fig. 10 (a).

$$\begin{bmatrix} A & B \\ C & D \end{bmatrix} = \begin{bmatrix} 1 & Z_{DSS} \\ 0 & 1 \end{bmatrix} \tag{23}$$

ABCD matrix shown in (23) can be converted to the scattering matrix in (24) through matrix conversion table [18].

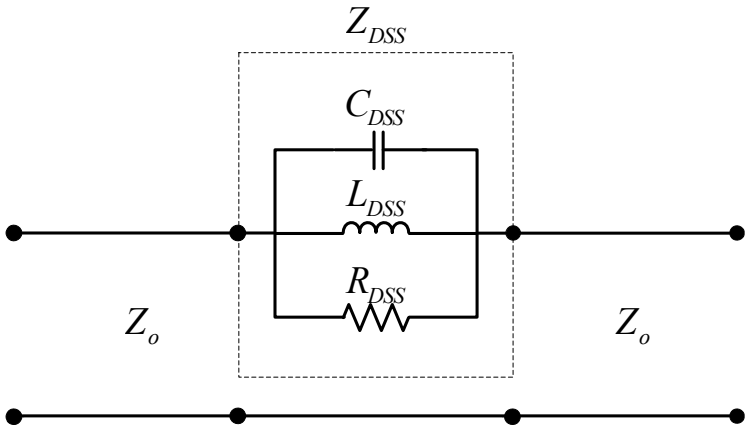

(a)

Fig. 10. (a) Complete equivalent circuit model of a DSS and (b) corresponding section.

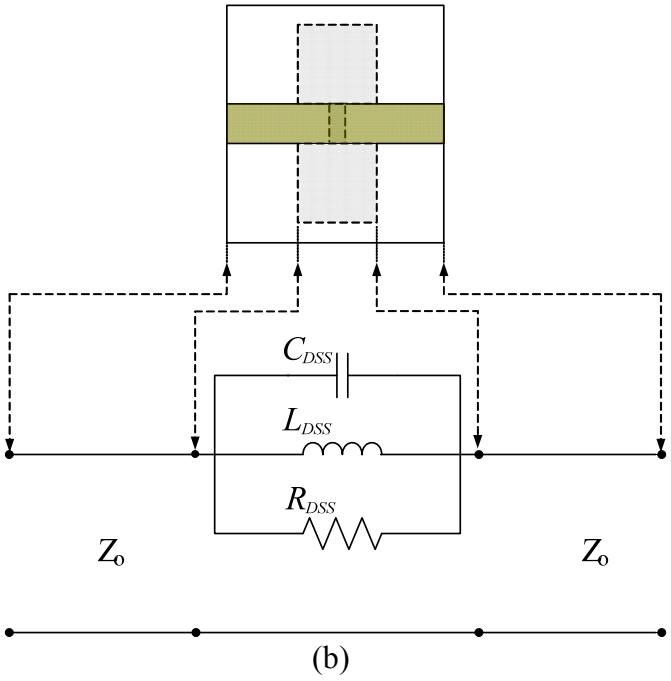

(b)

Fig. 10. Continued.

$$\begin{bmatrix} S_{11} & S_{12} \\ S_{21} & S_{22} \end{bmatrix} = \begin{bmatrix} \dfrac{Z_{DSS}}{Z_{DSS}+2Z_o} & \dfrac{2Z_o}{Z_{DSS}+2Z_o} \\ \dfrac{2Z_o}{Z_{DSS}+2Z_o} & \dfrac{Z_{DSS}}{Z_{DSS}+2Z_o} \end{bmatrix} \tag{24}$$

Since $Z_{DSS} = R_{DSS}$ at resonance ($\omega = \omega_o$), S_{21} in (24) can be expressed as (25).

$$R_{DSS} = \frac{2Z_o\left(1-S_{21}\right)}{S_{21}} \tag{25}$$

With the definition of the insertion loss in (26), (25) can be shown as (27)

$$IL_o\left(dB\right) = 20\log\left(1/S_{21}\right) \tag{26}$$

$$R_{DSS} = \frac{2\cdot Z_o(1-10^{\left\lfloor \frac{IL_o(dB)}{20} \right\rfloor})}{10^{\left\lfloor \frac{IL_o(dB)}{20} \right\rfloor}} \tag{27}$$

The insertion loss is found as 27dB, i.e., $-20\cdot\log(S_{21})=27dB$ in Fig. 9, so S_{21} is determined as 0.0446 by (26). Thus, R_{DSS} is also determined as 2142.2 ohm by (27). Finally, the resulting lumped equivalent circuit model is shown in Fig. 10 (b).

For the slot dimension of d=5 mm and g=0.7mm, C_{DSS}, L_{DSS}, and R_{DSS} are found as 0.096 pF, 3.4072 nH, and 2142.2 ohm, respectively. To prove the validity of the lumped equivalent circuit model, the measured result and circuit simulation result are compared with each other. Figure 11 shows that the simulation result of the complete equivalent circuit model and measured result of its corresponding dimensions of d=5 mm and g=0.7 mm. As shown in Fig. 11, the circuit simulation and measurement show very good agreement. Thus, the accuracy of the equivalent circuit extracting method of DSS is proved.

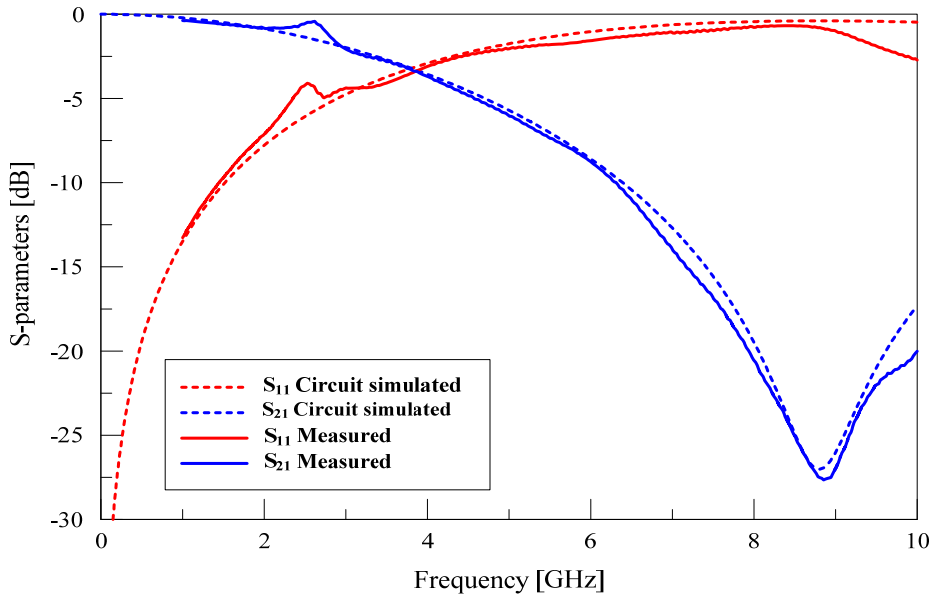

Fig. 11. Circuit simulation of the complete equivalent circuit model and measurement of DSS with the dimensions of d=7.5mm and g=0.3mm.

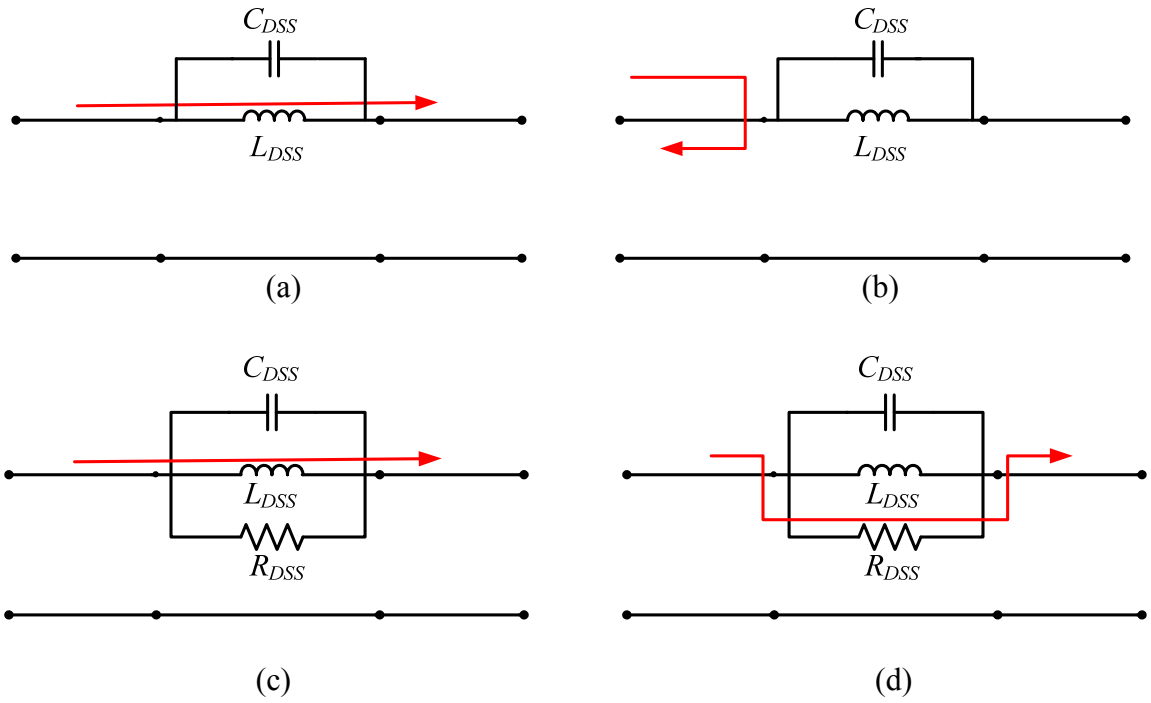

Fig. 12. The current flow in an equivalent circuit model of a slotted ground section: "Conventional model in lossless – (a) and (b)" and "Proposed model with losses – (c) and (d)".

Figure 12 (a) shows the current flows of the conventional equivalent circuit model in low frequency ranges (pass-band) where an inductance is dominant. The impedance in Fig. 12 (b) is infinity at resonance, so the incident power is reflected back to the input. The inductance of the proposed model in Fig. 12 (c) is also dominant, so the current flows along the inductance in low frequency ranges. Since the reactance is infinity in Fig. 12 (d), the resistance is dominant. Thus, the currents flow along the resistor.

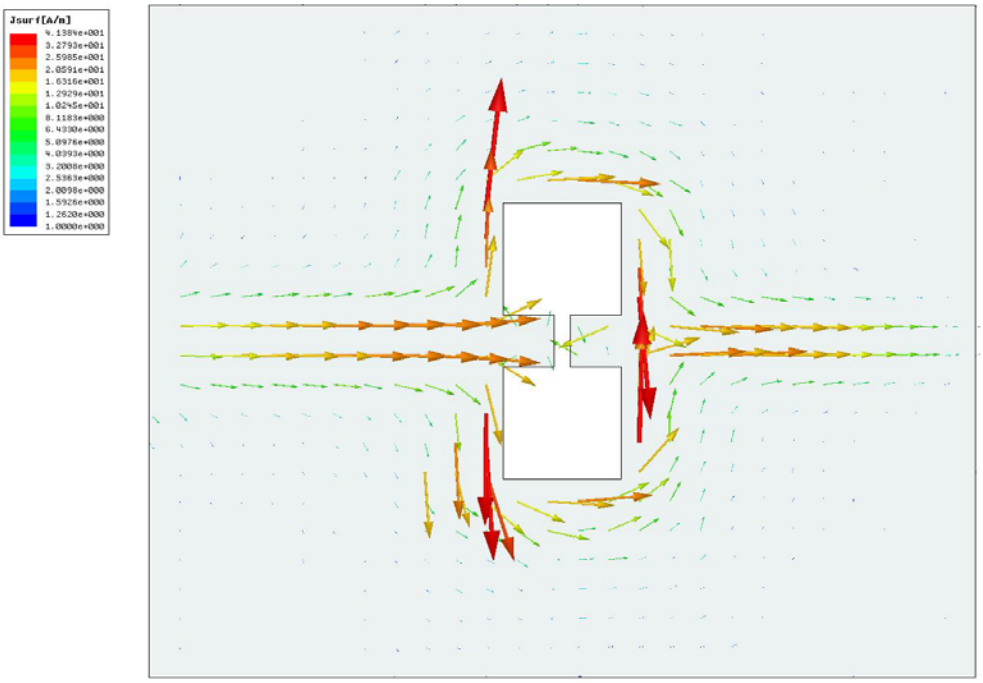

(a)

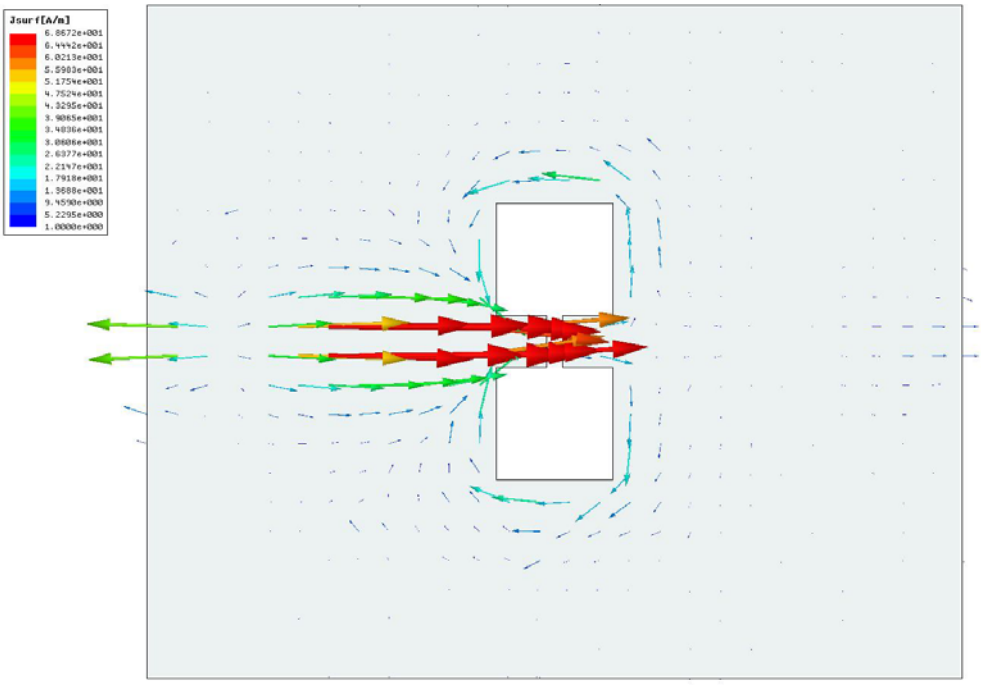

(b)

Fig. 13. The current distributions of the slotted ground with the dimensions of d=7.5 mm and g=0.3 mm at (a) pass-band and (b) stop-band.

In Fig. 13 (a), the currents flows along the square slotted area, and that makes the currents travels more distance. As a result, the longer current travel distance produces the corresponding amount of inductance in lower frequency range, i.e., pass-band. This also makes a sense in the impedance view point. For a parallel *LC* resonator, an inductance becomes dominant in low frequency range because the impedance of a capacitance is infinity in the low frequencies. As a result, the currents only flow along the square slotted area that produces the inductance. Figure 13 (a) shows the characteristic of the current flows when a slotted ground structure with dumbbell shape has the inductance dominant characteristic in low frequency range. As it is shown in Fig. 13 (a), the currents do not flow on a gap area since the impedance of the capacitance of the parallel *LC* resonator is infinity in low frequencies. In the other case, the capacitance becomes dominant as the frequency goes up. Figure 13 (b) shows that the current distributions of the slotted ground structure in high frequency range, i.e., stop-band. Since the impedance of the inductance of the parallel *LC* resonator goes infinity, as the frequency increases, the currents only flow through the gap. At resonant frequency, parallel LC resonator is open circuit so all current can not pass the slotted ground section. From Fig. 13 (a) and (b), one can expect that slotted area produces the inductance and the gap connecting two slot section generates the capacitance.

C. Curve Fitting Analysis of DSS

As shown in Fig. 14, the dumbbell shaped slot dimensions of g=0.2 mm and d=5 mm on substrate Duroid 5880 (ε=2.2, h=30 mil) produces the cutoff frequency and resonant frequency of 3.9 GHz and 7.2 GHz, respectively. From the frequency characteristics, the capacitance and inductance are determined as 0.1694 pF and 2.8836 nH by (18) and (19). Once a capacitance and an inductance are found from certain slot dimensions, other capacitances and inductances can be determined by varying the slot dimensions through EM simulation. The loss of slotted area is not considered for simplicity.

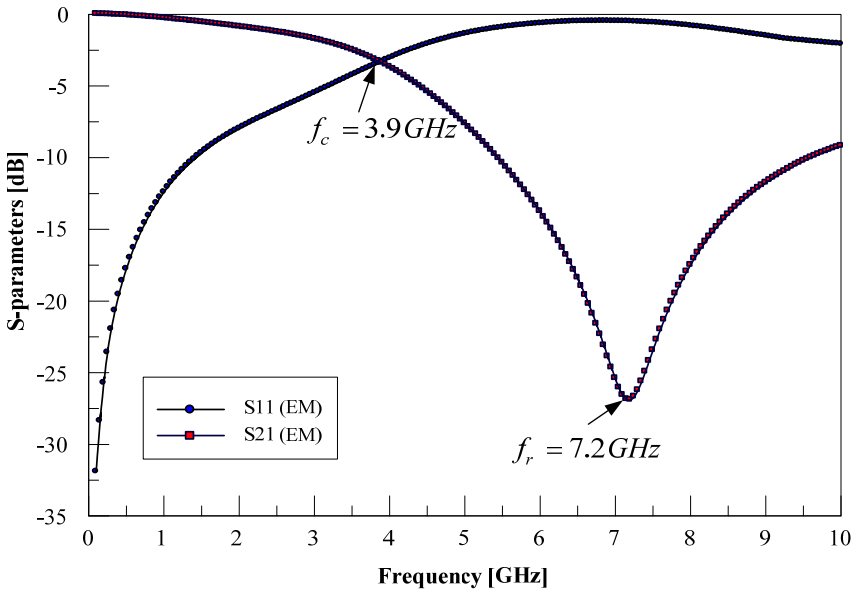

Fig. 14. EM simulated frequency response characteristics with a slot dimensions of d=5 mm and g=0.*2* mm.

As previously mentioned, the two square slot ($d\times d$) areas and the rectangle gap slot ($g\times d$) produce the inductance and capacitance, respectively. It is interesting to

calculate the gap capacitance versus the gap dimensions, while the inductance remains constant. This means that the two square slot dimensions do not change but the gap distance (g) varies. Varying the gap dimensions changes the resonant frequencies of the parallel LC resonator, so the gap capacitances can be calculated from the fixed inductance and varying resonant frequencies. Likewise, the inductance versus the slot dimensions can be calculated from the fixed gap capacitance and varying resonant frequencies. The curve fitting data is based on the substrate of Duroid 5880 (thickness=30 mil, ε_r=2.2). Later these slot dimensions for a LPF are determined by these curve fitting graphs.

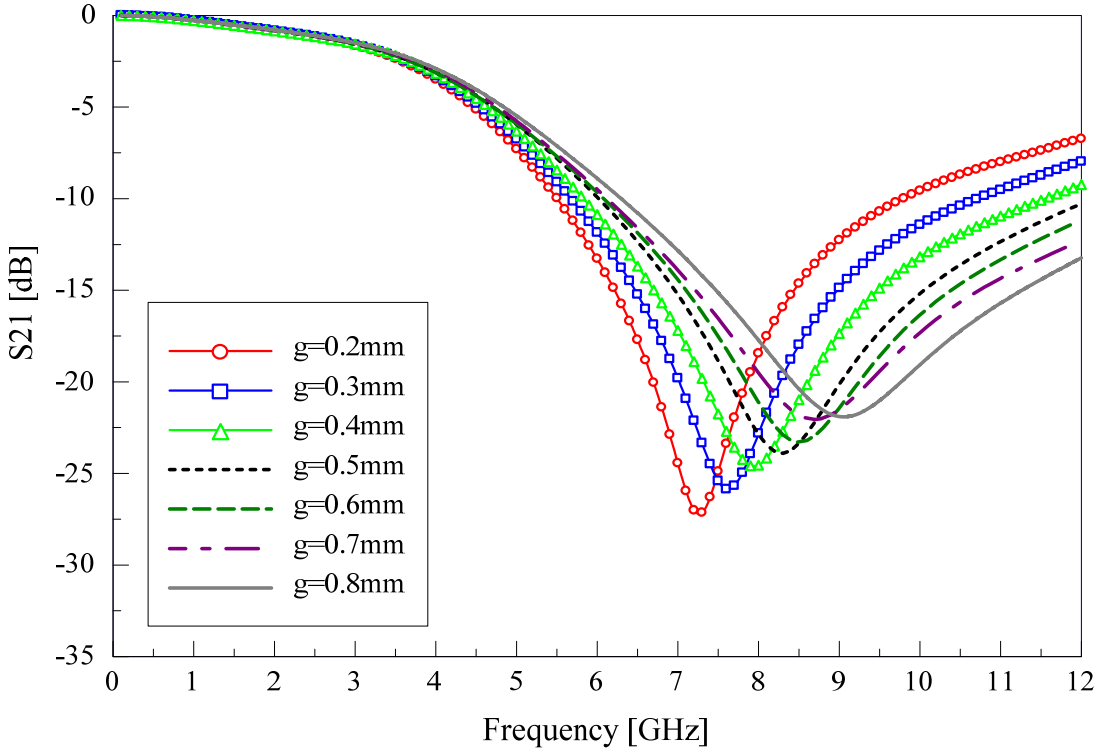

Fig. 15. EM simulation depending on different gap dimensions; the slot dimension is fixed as d=5 mm (2.8836 nH).

Figure 15 shows that the different resonant frequencies with varying gap dimensions. As the gap distance is bigger and bigger, the resonant frequency increases. This means that the capacitance decreases. In Fig. 15, the 3 dB cutoff point of S_{21} slope is not varied, which means that the inductance does not change even though the gap dimensions vary. Thus, varying the gap dimensions only changes the capacitance of the equivalent circuit model of a dumbbell shaped slot. Magnitudes of S_{21} at resonance also decrease as the gap dimensions are bigger. This could be explained as a resistance concept. As the insertion loss decreases, R_{DSS} also decreases from (27). Thus, the more currents can flow along the resistance path as the resistance (R_{DSS}) gets smaller and smaller.

Table 2. Capacitance variations with varying gap dimensions

Gap Dimension	Resonant Frequency (GHz)	Capacitance (pF)
0.2 mm × 2.3 mm	7.2	0.169
0.3 mm × 2.3 mm	7.7	0.148
0.4 mm × 2.3 mm	8.0	0.137
0.5 mm × 2.3 mm	8.3	0.127
0.6 mm × 2.3 mm	8.5	0.121
0.7 mm × 2.3 mm	8.7	0.116
0.8 mm × 2.3 mm	9.1	0.106

From the data in Table 2, a curve fitting graph of the capacitance versus gap dimensions can be plotted as shown in Fig. 16. Since its slope shows the approximately linear variation, equation (28) can be used to describe the linear curve shown in Fig. 16.

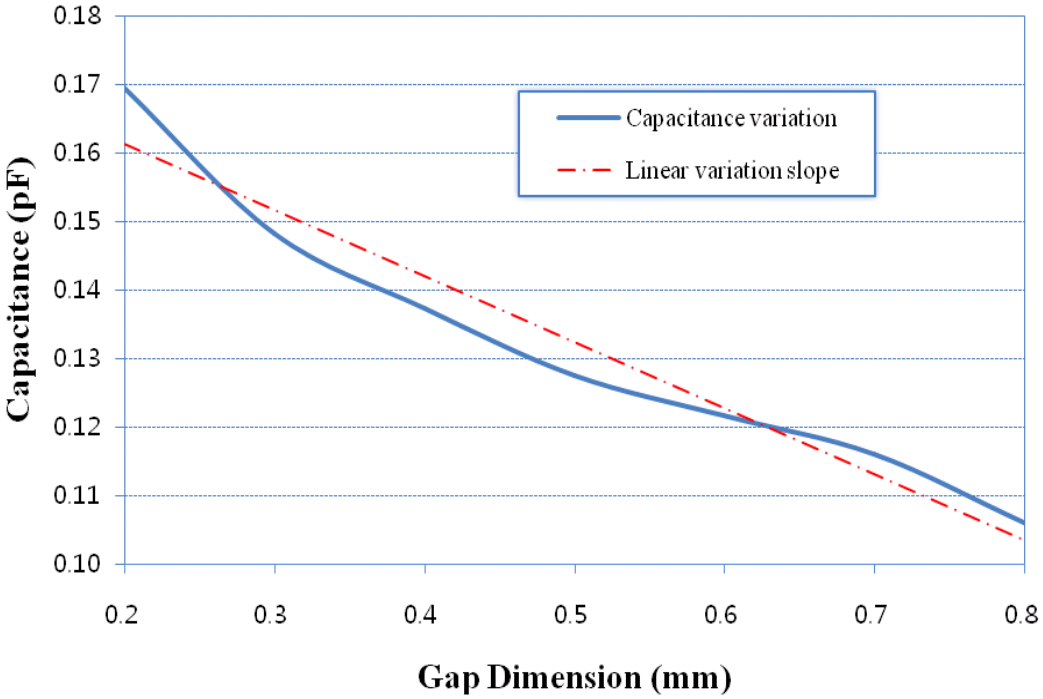

Fig. 16. Capacitance curve fitting graph with the varying gap dimensions.

$$C_{DSS}\ (pF) = -0.096 \cdot g\,(mm) + 0.18 \tag{28}$$

One can instantly calculate the equivalent capacitance from (28) by giving the gap dimensions.

Figure 17 shows that the different resonant frequencies with varying slot dimensions. As the slot dimensions are bigger and bigger, the resonant frequencies decreases. This presents that as the slot dimensions increase, an inductance due to the slot dimensions also increases. Thus, the resonant frequency decreases because of increased inductance.

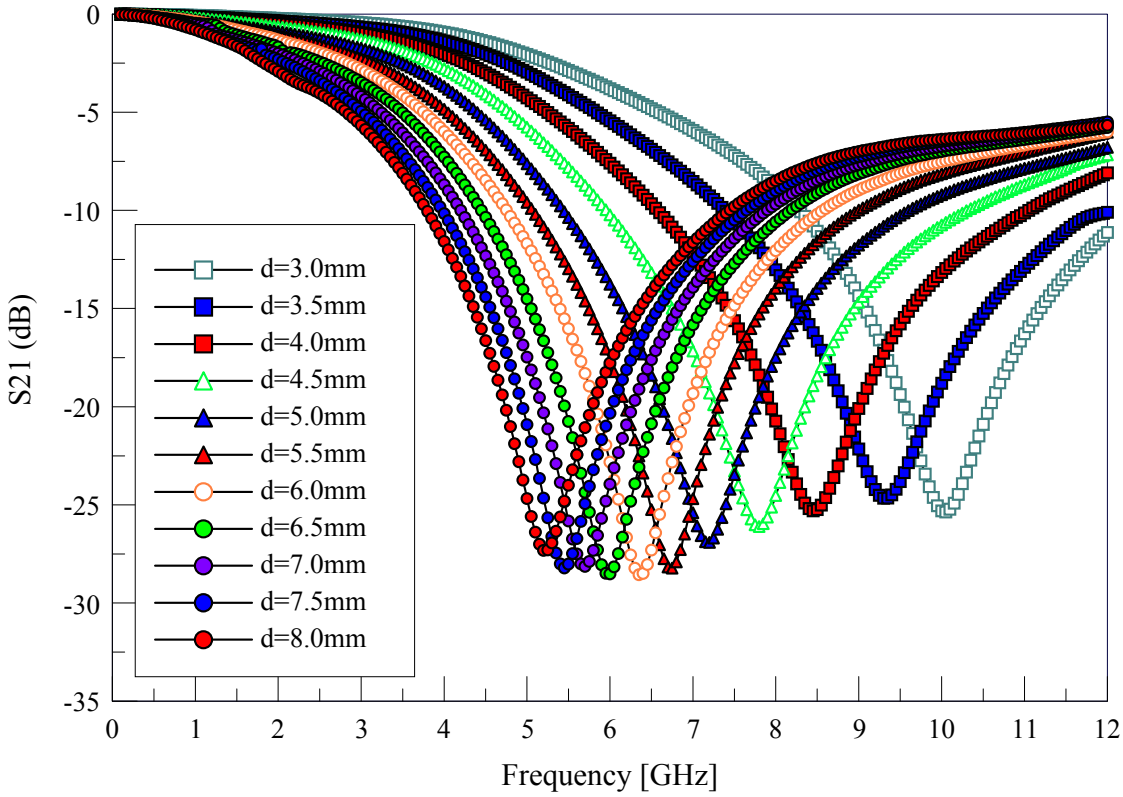

Fig.17. EM simulation depending on the different slot dimensions; the gap dimension is fixed as *g*=0.2 mm (0.1694 pF).

Table 3. Inductance variations with varying slot dimensions

Slot Dimension	Resonant Frequency (GHz)	Inductance (nH)
3.0 mm × 3.0 mm	10.05	1.480
3.5 mm × 3.5 mm	9.35	1.710
4.0 mm × 4.0 mm	8.50	2.070
4.5 mm × 4.5 mm	7.80	2.457
5.0 mm × 5.0 mm	7.20	2.883
5.5 mm × 5.5 mm	6.75	3.281
6.0 mm × 6.0 mm	6.40	3.650
6.5 mm × 6.5 mm	6.00	4.152
7.0 mm × 7.0 mm	5.70	4.601
7.5 mm × 7.5 mm	5.50	4.941
8.0 mm × 8.0 mm	5.25	5.423

From the data in Table 3, Fig. 18 which is the curve fitting graph of the inductance versus slot dimensions can be plotted. Since its slope shows the linear variation, (29) can be also written for the curve shown in Fig. 18.

$$L_{DSS}\ (nH) = 0.7886 \cdot d(mm) - 0.974 \tag{29}$$

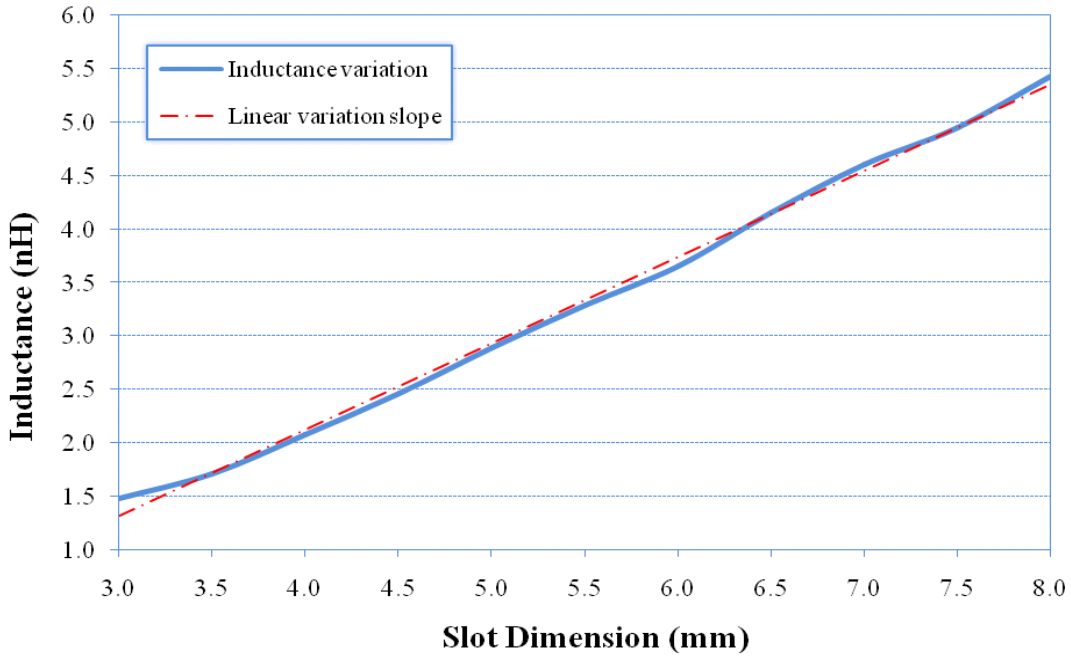

Fig. 18. Inductance curve fitting graph with the varying slot dimensions.

The equivalent inductance depends on the slot dimensions. The bigger slot dimensions give the larger inductance. One can instantly calculate the equivalent inductance from (29) by giving the slot dimensions.

CHAPTER IV

PERIODIC STRUCTURE ANALYSIS

A. Equivalent Circuit of Periodic DSS

An infinite transmission line or waveguide periodically loaded with reactive elements or discontinuities is referred to as a periodic structure [19]. Wave propagation through various periodic structures has attracted many researchers' interests [20, 21] and their applications are found in filters, antennas, and waveguides [22]-[25]. Two interesting properties in all periodic wave-guiding structures are following [26]: (a) they exhibit pass-band/stop-band characteristics and (b) they can support slow wave propagations whose phase velocities are less than the velocity of light. These properties can be briefly explained by transmission line theory. The propagation constant and phase velocity in a lossless transmission line are defined as $\beta = \omega\sqrt{LC}$ and $v_p = 1/\sqrt{LC}$, respectively. Here L and C in these two equations are the characteristic inductance and capacitance of a transmission line per unit length. Increasing these inductance and capacitance by loading reactive elements or placing discontinuities the phase velocity of the transmission line can be decreased. Thus, the increased propagation constant, β makes the phase velocity less than speed of light in (30). In this case, the ratio k/β is less than the unity, which results in slow wave propagation where the unloaded propagation constant, k, is less than the loaded propagation constant, β.

$$v_p = \frac{1}{\sqrt{LC}} = \frac{\omega}{\beta} = c\frac{k}{\beta} \tag{30}$$

Pass/stop-bands can be also determined through the transmission line theory and cascaded network analysis technique. From the analysis, the propagation constant in periodic structures is solved by two different conditions which produce the propagation ($\alpha = 0,\ \beta \neq 0$) or attenuation ($\alpha \neq 0,\ \beta = 0$). This is very useful to define the pass/stop-bands in a periodic structure. Since a periodically load line exhibits the pass/stop-band, it can be considered as a filter. Even though the frequency response of the periodic structures is similar to a filter, they may not be suitable for the modern filter design. The periodic structures have the drawbacks in size, pass/stop-band characteristics, and loss. It is also difficult to design a periodic structure filter from given specifications such as cutoff frequency, pass/stop-band characteristics, and bandwidth.

In this section, analytical techniques and mathematical derivations are presented to investigate the periodic structure with a dumbbell shaped slots in the ground plane. *Brillouin* diagram, so called $k - \beta$ *diagram,* is shown to predict the pass/stop-bands.

Figure 19 shows the periodic structure constructed in microstrip. Dumbbell shaped slots are periodically loaded with a certain distance in the ground plane. As studied earlier, this dumbbell shaped slot is considered as pure reactive elements in a lossless case. Figure 20 shows its equivalent circuit model consisted of *LC* parallel resonators and transmission lines. C_{DSS} and L_{DSS} are the capacitances and inductances produced by each dumbbell shaped slot. *L* presents the distance between two adjacent resonators. *k* is defined as the propagation constant of a unloaded line in (31).

$$k = \frac{\omega}{c} \cdot \sqrt{\varepsilon_{eff}} = \frac{2\pi}{\lambda_o} \cdot \sqrt{\varepsilon_{eff}} \tag{31}$$

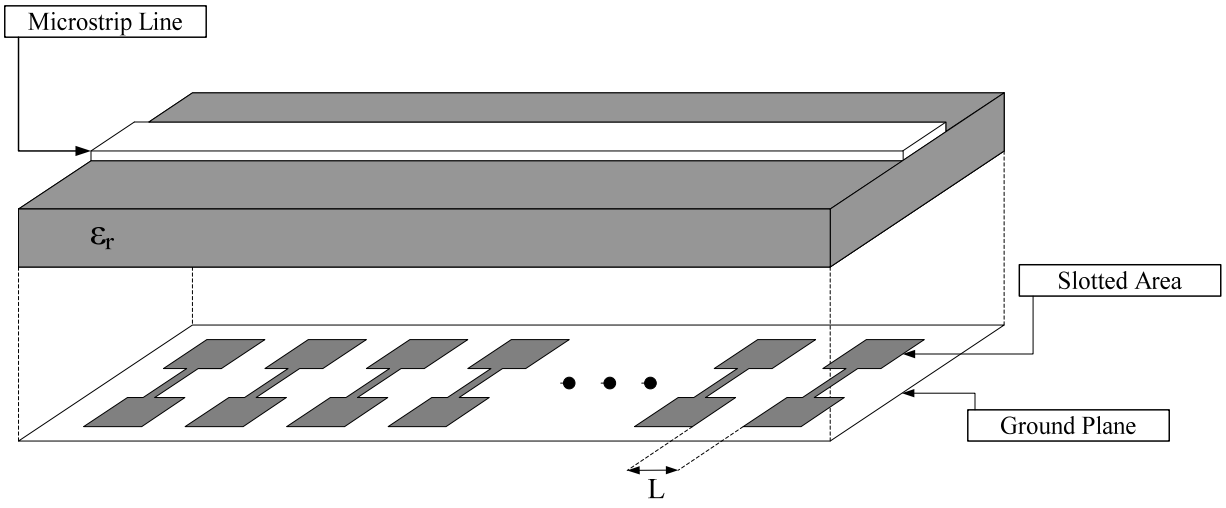

Fig. 19. 1D-periodic structure with dumbbell shaped slots in the ground plane.

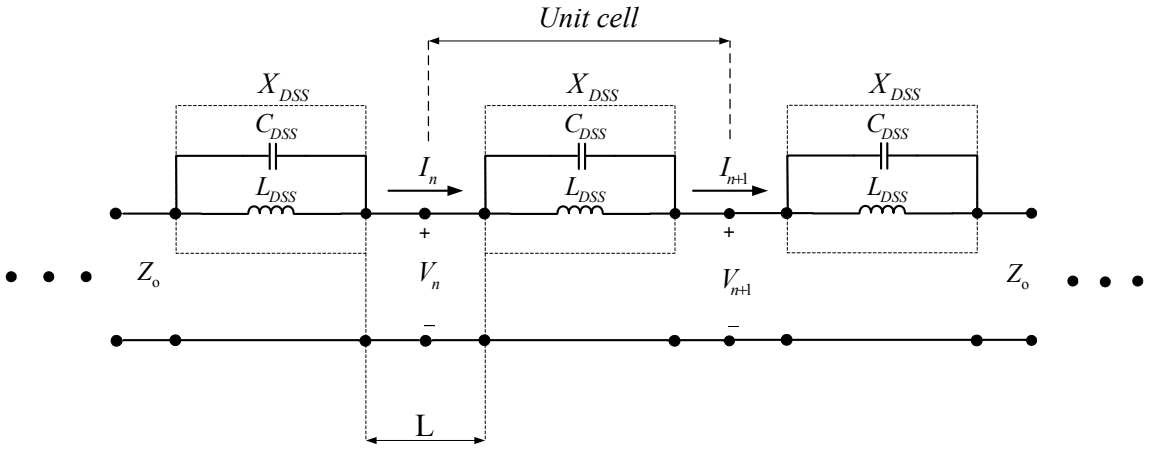

Fig. 20. Equivalent circuit model of 1D-periodic structure with dumbbell shaped slots in the ground plane.

B. k-β Diagram of Periodic DSS

For a cascaded network shown in Fig. 20, a single unit cell can be expressed as (32) by using transmission line theory. In (32), transmission line's electrical length is expressed as $\theta = k \cdot L$.

$$\begin{bmatrix} A & B \\ C & D \end{bmatrix} = \begin{bmatrix} \cos\frac{\theta}{2} & jZ_o \sin\frac{\theta}{2} \\ j\frac{1}{Z_o}\sin\frac{\theta}{2} & \cos\frac{\theta}{2} \end{bmatrix} \begin{bmatrix} 1 & jX \\ 0 & 1 \end{bmatrix} \begin{bmatrix} \cos\frac{\theta}{2} & jZ_o \sin\frac{\theta}{2} \\ j\frac{1}{Z_o}\sin\frac{\theta}{2} & \cos\frac{\theta}{2} \end{bmatrix} \tag{32}$$

By using the half angle equation in (33), (32) can be shown as (34). *ABCD* matrix in (34) presents the single unit cell of dumbbell shaped slot. Since *A*=*D* and *AD*-*BC*=1 in (34), the single unit cell is symmetrical and reciprocal, respectively. *A* and *D* are real and *B* and *C* are imaginary, therefore the network is lossless.

$$\begin{aligned} \sin\frac{\theta}{2} &= \pm\sqrt{\frac{1-\cos\theta}{2}} \\ \cos\frac{\theta}{2} &= \pm\sqrt{\frac{1+\cos\theta}{2}} \\ \sin\frac{\theta}{2}\cdot\cos\frac{\theta}{2} &= \frac{\sin\theta}{2} \end{aligned} \tag{33}$$

$$\begin{bmatrix} A & B \\ C & D \end{bmatrix} = \begin{bmatrix} \cos\theta - \frac{X}{2\cdot Z_o}\sin\theta & j\left(\frac{X}{2}\cos\theta + Z_o\sin\theta + \frac{X}{2}\right) \\ j\left(\frac{X}{2\cdot Z_o^2}\cos\theta + \frac{1}{Z_o}\sin\theta - \frac{X}{2\cdot Z_o^2}\right) & \cos\theta - \frac{X}{2Z_o}\sin\theta \end{bmatrix} \tag{34}$$

Since *ABCD* matrix explains the current and voltage relation of the input and output of the *n*th network, (36) can be derived from (35). Each term of ABCD matrix in (36) is defined as (37).

$$\begin{bmatrix} V_n \\ I_n \end{bmatrix} = \begin{bmatrix} A & B \\ C & D \end{bmatrix} \begin{bmatrix} V_{n+1} \\ I_{n+1} \end{bmatrix} = \begin{bmatrix} V_{n+1} \\ I_{n+1} \end{bmatrix} e^{\gamma L} \tag{35}$$

$$\begin{bmatrix} A - e^{\gamma L} & B \\ C & D - e^{\gamma L} \end{bmatrix} \begin{bmatrix} V_{n+1} \\ I_{n+1} \end{bmatrix} = 0 \tag{36}$$

In order to solve (36) in terms of V_{n+1} and I_{n+1}, (38) must be satisfied for nontrivial solution. If the determinant in (36) is not zero, the inverse matrix exists. Thus, one has the infinite number of solutions and this doesn't have any physical meaning.

$$\begin{aligned} A' &= A - e^{\gamma L} \\ B' &= B \\ C' &= C \\ D' &= D - e^{\gamma L} \end{aligned} \tag{37}$$

$$A'D' - B'C' = 0 \tag{38}$$

Equation (39) is obtained by substituting (37) into (38). From the original condition which is the reciprocal unit cell, (42) is derived through (40) and (41).

$$AD + e^{2\gamma L} - \left(A + D\right)e^{rL} - BC = 0 \tag{39}$$

$$AD - BC = 1 \tag{40}$$

$$e^{-\gamma L} + e^{rL} = A + D \tag{41}$$

$$\cosh(\gamma L) = \cosh(\alpha L)\cos(\beta L) + j\sinh(\alpha L)\sin(\beta L) = \frac{A + D}{2} \tag{42}$$

The right hand side of (42) is real, so either α or β should be zero. To solve (42), two different conditions are assumed as following: (a) propagating condition and (b) non-propagating condition in periodic structure.

(a): $\alpha = 0$ and $\beta \neq 0$. In this case, the phase constant, β becomes the propagation constant, i.e., $\gamma = +j\beta$. Equation (43) is obtained from (42) with the condition of $\alpha = 0$ and $\beta \neq 0$. This defines the pass-band.

$$\cos(\beta L) = \cos\theta - \frac{X}{2 \cdot Z_o}\sin\theta \tag{43}$$

(b): $\alpha \neq 0$ and $\beta = 0$ or $\beta \cdot \mathrm{L} = \pi$. In this case, when the phase constant is zero the attenuation constant, α becomes the propagation constant, i.e., $\gamma = \alpha$. Equation (44) is obtained from (42) with the condition of $\alpha \neq 0$ and $\beta = 0$. This defines the stop-band. Since the lossless condition is assumed, the most of input power is reflected back to input rather than dissipated. There is also the power radiated through slot discontinuities. In both cases of (a) and (b), the attenuation constant and phase constant are greater than zero, i.e. $\alpha > 0$ and $\beta > 0$, for the wave propagating in positive direction. With the condition of $\alpha \neq 0$ and $\beta \cdot L = \pi$, (45) is derived from (42). In this case, the distance between all reactive elements is $\lambda_g / 2$, thus an input impedance is the same with the condition of $\beta = 0$.

$$\cosh(\alpha L) = \cos\theta - \frac{X}{2 \cdot Z_o}\sin\theta \tag{44}$$

$$-\cosh(\alpha \cdot L) = \cos\theta - \frac{X}{2 \cdot Z_o}\sin\theta \leq -1 \tag{45}$$

By solving (43) and (44) in terms of $\beta \cdot L$ and $\alpha \cdot L$, $k - \beta$ *diagram* can be plotted in Fig. 21. Even though (42) and (43) are derived from a single unit cell, the $k - \beta$ *diagram* in Fig. 21 or 22 represents the periodic structure with the infinitely

loaded elements. When $\beta \cdot L$ is purely real, $\alpha \cdot L$ is purely imaginary, and this yields that the propagation constant, γ is purely imaginary ($\gamma = j\beta$), i.e., pass-band. When $\beta \cdot L$ is purely imaginary, $\alpha \cdot L$ is purely real, then this produces that γ is purely real ($\gamma = \alpha$), i.e., stop-band.

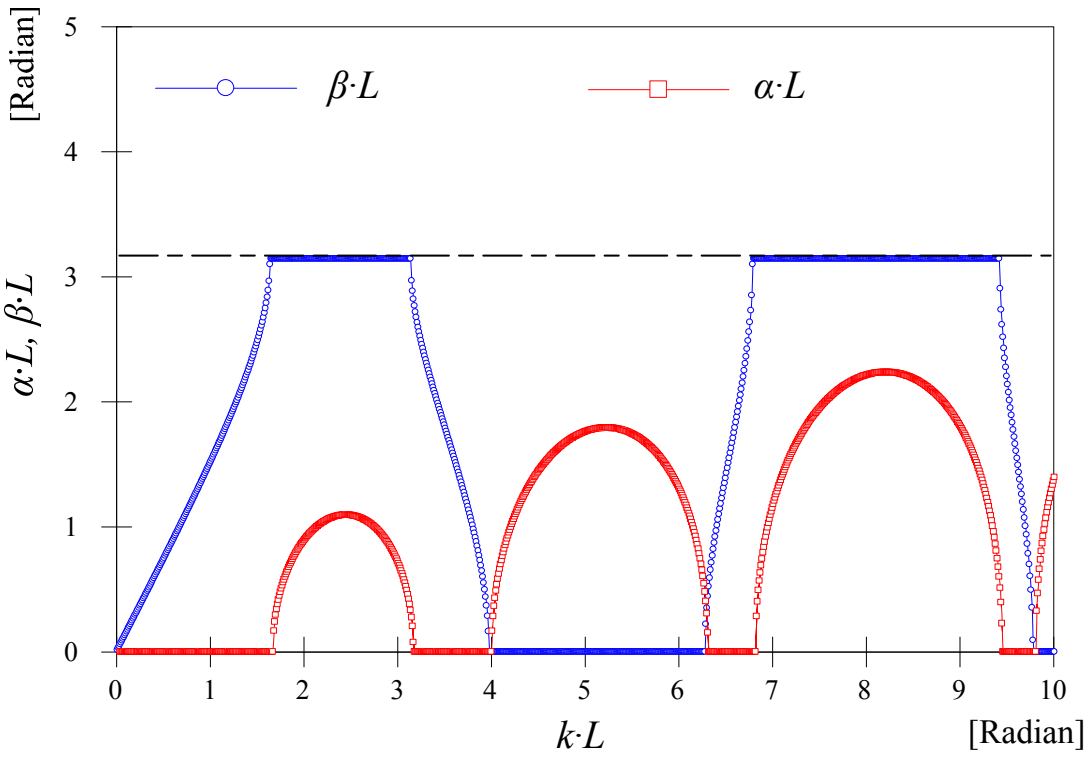

Fig. 21 $k-\beta$ *diagram* of the periodic structure with the infinite number of dumbbell shaped slots.

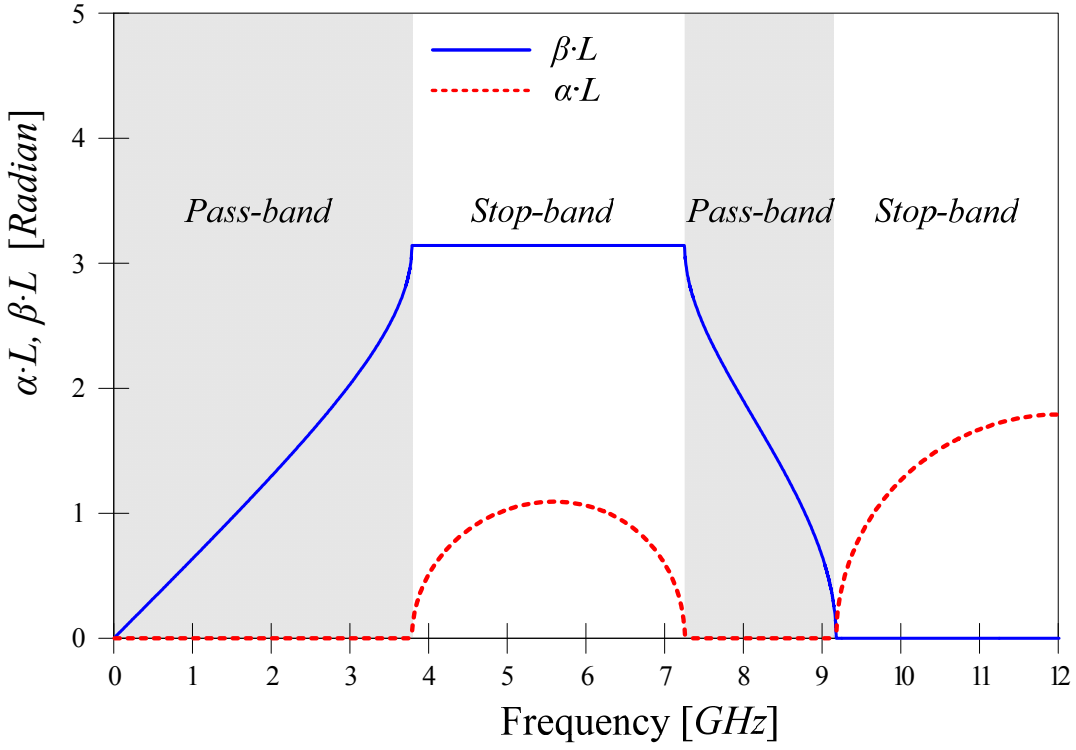

Fig. 22. Frequency versus $k-\beta$ *diagram* of the periodic structure with the infinite number of dumbbell shaped slots.

C. Simulation and Measurement

To validate the theory of the periodic structure, calculated and measured data are compared. Figure 23 shows the fabricated periodic structure with dumbbell shaped slots in the ground plane. Duroid 5880 ($\varepsilon_r = 2.2$) is used as substrate and its' thickness is 0.765 mm. The number of the slots are N=7 and the distance between adjacent slots is 15 mm. The dimensions of the dumbbell shaped slots are d=4.8 mm g=0.6 mm, which produce the inductance of 2.842 nH and capacitance of 0.123 pF, respectively. Figure 24 shows the circuit configurations (N=7) for simulation. The calculated and measured

results are compared in Fig. 25. The expected pass/stop-bands shown in Fig. 22 illustrate good agreement with the simulated results in Fig. 25, but the frequency response of measured results is shifted to the left about 500 Mhz as compared to calculated and simulated one.

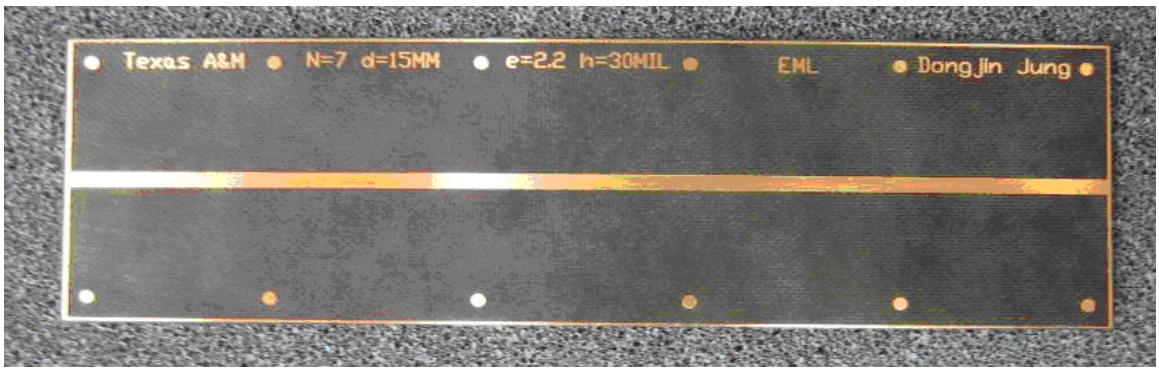

(a)

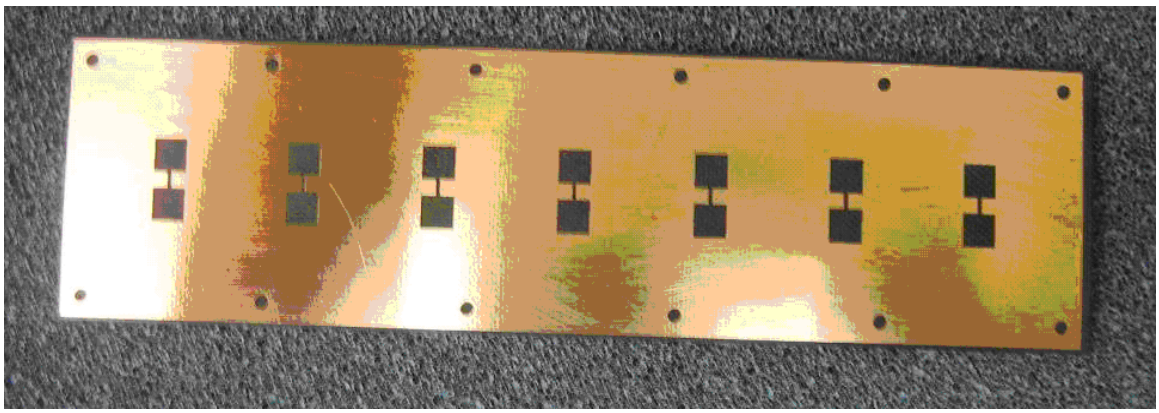

(b)

Fig. 23. Fabricated periodic structure with dumbbell shaped slots (*N*=7) (a) top view and (b) bottom view.

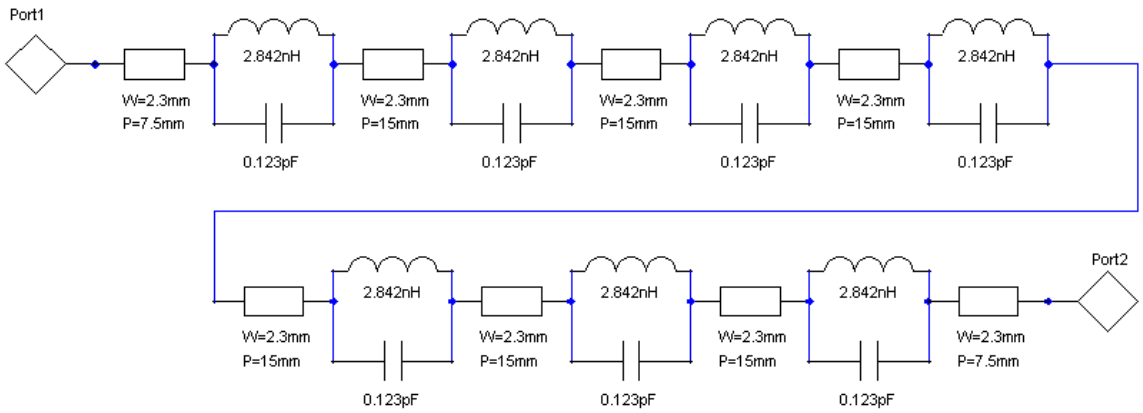

Fig. 24. Circuit simulation schematic using [27] Ansoft Designer v. 3.0.

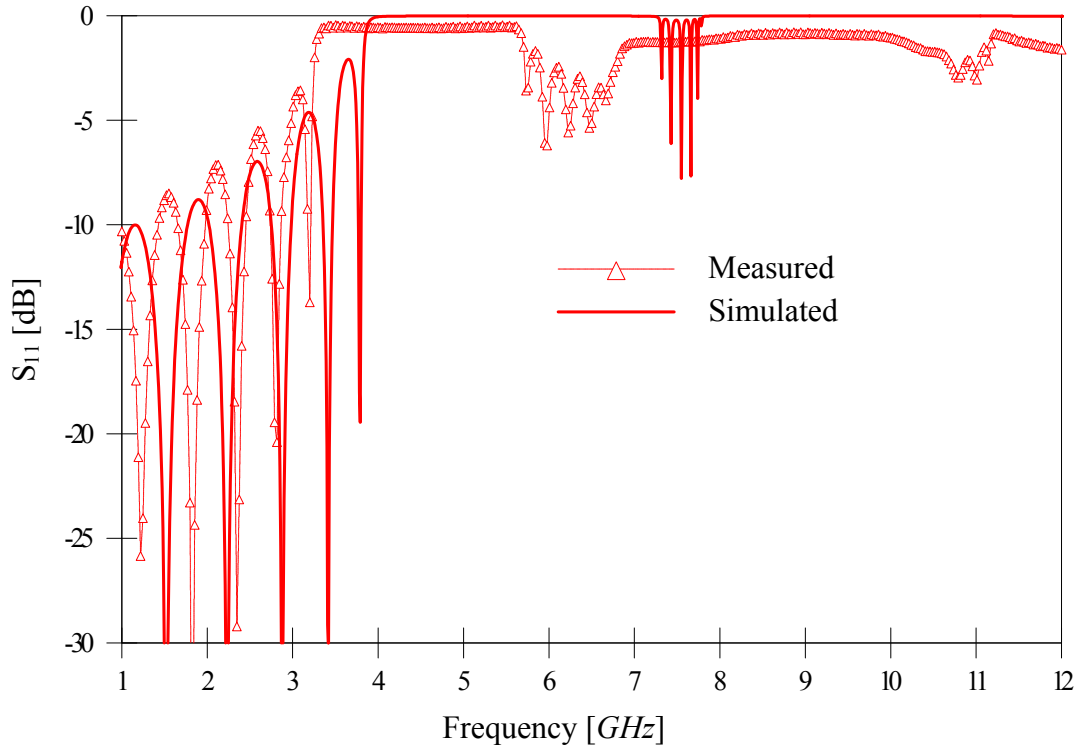

(a)

Fig. 25. Calculated and measured periodic structure with dumbbell shaped slots (N=7) (a) return loss and (b) insertion loss.

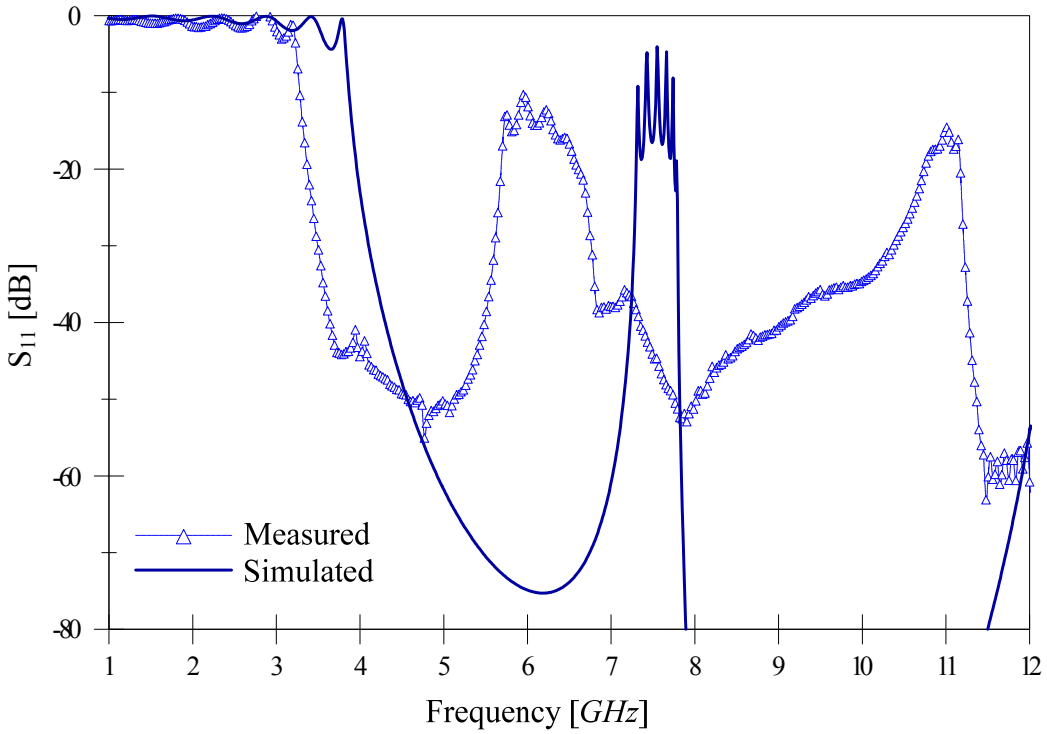

(b)

Fig. 25. Continued.

CHAPTER V

LOWPASS FILTER DESIGN WITH DUMBBELL SHAPED SLOT

A. Design Theory for Lowpass Filter with DSS

In the previous section, the slotted ground structure with a dumbbell shape has been studied and its equivalent circuit model also introduced. Based on insertion loss method filter theory, LPF can be designed by using this dumbbell shaped slot in the ground plane. This section begins with introducing the conventional LPF design with DS-SGS reported in [28]. Later, the proposed technique to improve the conventional method is also presented. The drawback to this conventional method using two slotted ground sections and one parallel stub is that the parasitic inductance of the parallel stub is not accounted for, producing errors in the cutoff frequency. This error is tolerable for a filter with a single parallel stub, but many filters feature multiple sections to provide a sharper cutoff. For these filters, the conventional LPF design methodology with the slotted ground is insufficient. In order to improve the accuracy of the LPF design with the slotted ground, this thesis provides a technique for addressing the otherwise ignored parasitic inductance.

In this proposed analysis technique, the inductance, which is one of the equivalent circuit components of a DSS, is recalculated by the modified inductance equation. The modified inductance equation excludes the additional inductance effect from the parallel stub since the parasitic inductance of the parallel stub is subtracted from the initial inductance of the DSS dimensions. This means that the slot dimensions

of the DSS should be readjusted to compensate for the parasitic inductance from the parallel stub. The curve fitting graphs representing the inductance and capacitance versus the different slot dimensions are plotted through the computer aided EM analysis. By using these curve fitting plots, the DSS dimensions are estimated and applied to the LPF design with the dumbbell shaped slot.

To compare the conventional and proposed methods, this thesis suggests a π-type LPF utilizing two parallel stub sections and a single DSS on the ground plane. The desired 3 dB cutoff frequency and the number of filter stages are f_c= 4.2 GHz and N=3, respectively. The accuracy of the proposed method is demonstrated by comparing the simulated and measured results. Circuit and EM simulation in the proposed method show good agreement with measured data.

In this section, two π-type LPFs are designed, simulated, and measured in order to compare the conventional and proposed methods. Both design techniques are based on a maximally flat type LPF design theory because the frequency response characteristics of a single DSS and a maximally flat type LPF (N=1) are the same. In the conventional LPF design with the dumbbell shaped slot, EM simulation is performed first to determine the cutoff and resonant frequencies of a DSS, from which equivalent circuit components are calculated. Finding the cutoff and resonant frequency information from EM simulation is not an efficient way to design a LPF with a DSS. This conventional procedure is also not convenient for designing a LPF with a randomly defined cutoff frequency. The equivalent inductance and capacitance need to be calculated from the specified design cutoff frequency for design convenience. This method is introduced in

(17), (46) and (47), which can be found in [12]. Equation (47) still has two unknown parameters, ω_r and L_{DSS}, even though ω_c has been determined. To make the conventional design equations simpler, $\omega_r=2\omega_c$ is defined. Setting $\omega_r=2\omega_c$ is a suitable assumption for keeping good pass-band and stop-band characteristics. With $\omega_r=2\omega_c$, (47) can be simplified to (48).

$$Y_{DSS} = Y_L = \frac{1}{g_1 Z_o} = -\omega_c C_{DSS} + \frac{1}{\omega_c L_{DSS}} \tag{46}$$

$$\omega_c = -\frac{\omega_r^2 \cdot L_{DSS}}{2 \cdot g_1 \cdot Z_o} \pm \sqrt{\left(\frac{\omega_r^2 \cdot L_{DSS}}{2 \cdot g_1 \cdot Z_o}\right)^2 + \omega_r^2} \tag{47}$$

$$L_{DSS} = \frac{3}{4\omega_c}\left(g_1 \cdot Z_o\right) \tag{48}$$

The proposed equation (48) enables one to determine the desired cutoff frequency first and calculate the equivalent inductance without EM simulation. Once the equivalent inductance is found, the equivalent capacitance can be calculated from (19), where $\omega_r=2\omega_c$. At this point, two LPFs with f_c=4.2 GHz and N=3 are designed by using the conventional and proposed methods. The resonant frequency of a DSS is set to 8.5 GHz ($\approx 2f_c$) for convenience. Since f_c and f_r are determined, C_{DSS} and L_{DSS} can be determined: L_{DSS}=2.842 nH and C_{DSS}=0.123 pF from (48) and (19). Once C_{DSS} and L_{DSS} are known, the DSS dimensions can be found from the inductance and capacitance curve fitting plots in Fig. 16 and Fig. 18. Curve fitting graphs give the DSS dimensions of d=4.8 mm and g=0.6 mm in order to produce the equivalent inductance and capacitance. In Fig. 26, EM simulation of the DSS (d=4.8 mm, g=0.6 mm) and its lumped equivalent circuit model simulation show very good agreement, which proves the validity of the

modified equivalent circuit extracting method. The desired cutoff frequency of 4.2 GHz and resonant frequency of 8.5 GHz are shown in Fig. 26. The DSS dimensions (d=4.8 mm and g=0.6 mm) can be immediately used for the LPF design because the cutoff characteristic matches that of a maximally flat type LPF with the cutoff frequency of 4.2 GHz and N=1. The DSS in the ground plane replaces the series inductance of the lumped prototype LPF model.

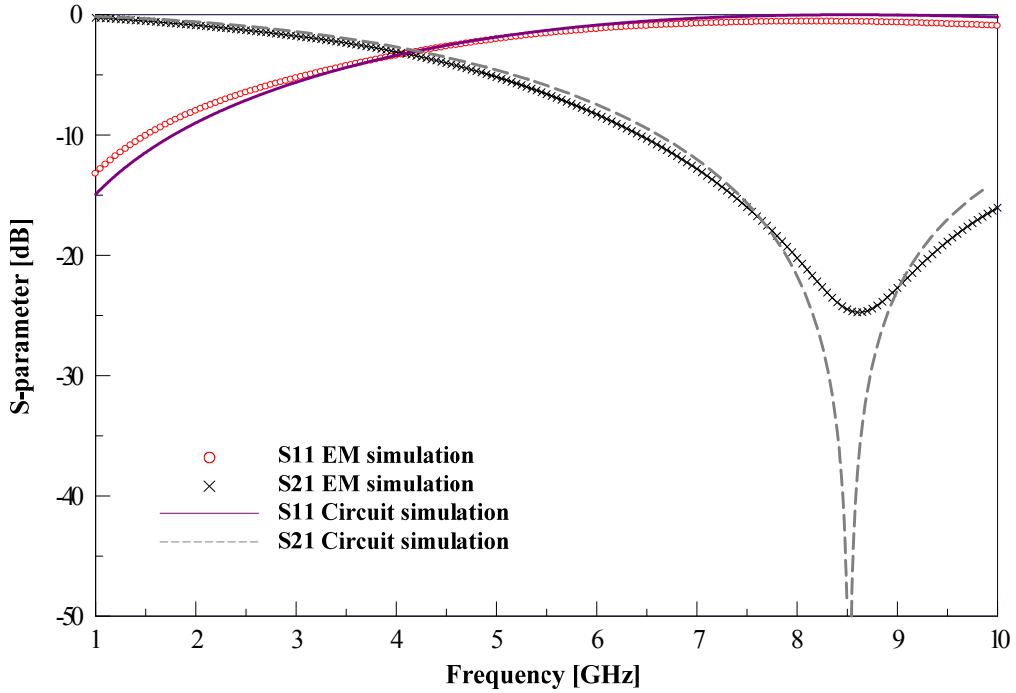

Fig. 26. EM and the equivalent circuit simulations of the single DSS with the dimensions of d=4.8 mm and g=0.6 mm.

B. Conventional Lowpass Filter Design with DSS

A maximally flat type LPF with N=3 and f_c=4.2 GHz is designed by using the well-known filter theory shown in Fig. 27(a). From the given cutoff frequency of f_c=4.2 GHz, C_1=C_3=0.757 pF and L_2=3.79 nH are found using (49) and (50).

$$L_k = \frac{g_k Z_o}{\omega_c} \tag{49}$$

$$C_k = \frac{g_k}{\omega_c Z_o} \tag{50}$$

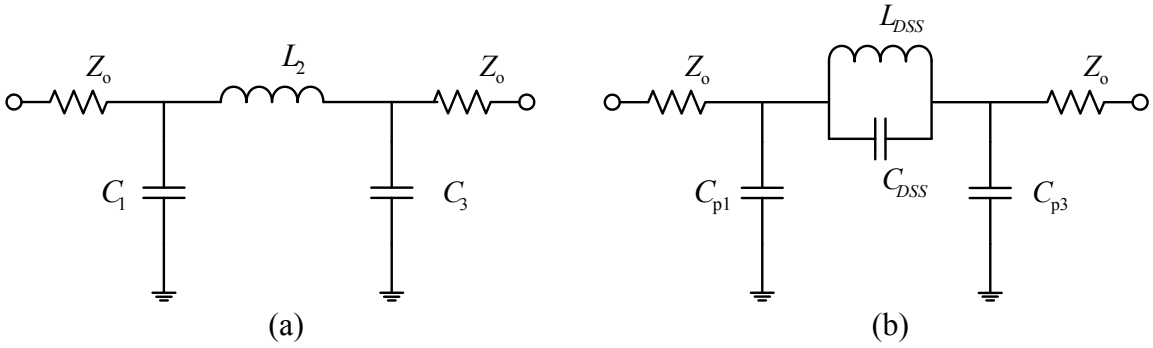

Fig. 27. The lumped equivalent circuit models of (a) a prototype LPF and (b) a conventional LPF with a dumbbell shaped slot.

The lumped equivalent circuit configuration of a LPF with a dumbbell shaped slot is shown in Fig. 27 (b), where L_{DSS} and C_{DSS} are derived to be equivalent with L_2 according to (17) and as found in L_{DSS}=2.842 nH and C_{DSS}=0.123 pF through (48) and (19). Parallel capacitances, C_{p1} and C_{p3} are the same as C_1 and C_3. Because the lumped equivalent circuit models of (a) the prototype LPF and (b) the LPF with a dumbbell shaped slot, as shown in Fig. 27, are designed to produce the same cutoff frequency of

4.2 GHz, they must show the same frequency response in circuit simulation. Circuit simulation of Fig. 27 (a) is the standard of a maximally flat type LPF with N=3 and f_c=4.2 GHz, so the agreement between the two LPF models reveals the reliability of a LPF with a dumbbell shaped slot and its lumped equivalent circuit model. Figure 28 shows the frequency response characteristics of the models in Fig. 27 (a) and (b). The 3 dB cutoff frequencies of these two models occur at 4.2 GHz exactly, and the frequency responses match in the pass-band. The anti-resonant frequency of the rejection-band occurs at 8.52 GHz in the LPF model with a dumbbell shaped slot. This resonant frequency is produced by the parallel LC resonator (L_{DSS} and C_{DSS}) of the equivalent circuit model with a dumbbell shaped slot.

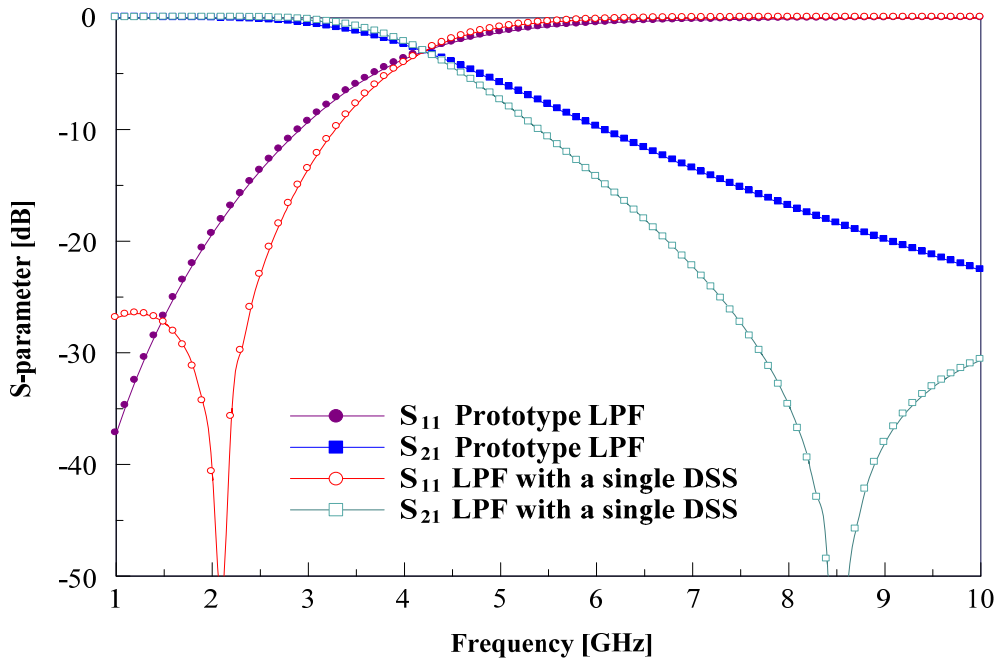

Fig. 28. The circuit simulation of the prototype LPF and the equivalent circuit of a LPF with a dumbbell shaped slot.

Thus, it has been proven that the lumped equivalent circuit model of the conventional LPF with a dumbbell shaped slot is accurate enough compared to its standard model. Although the lumped model is transformed to the distributed circuit by using the conventional LPF method with a dumbbell shaped slot, the frequency response should be also accurate enough to validate its conventional design theory.

Now the distributed model of the LPF with a dumbbell shaped slot is designed through the conventional method introduced in [28]. To design the equivalent distributed model of Fig. 27 (b), the DSS dimensions on the ground should be defined to realize the equivalent *LC* parallel resonator. With its calculated inductance and capacitance, this dimension can be instantly found from the curve fitting graphs in Fig. 16 and Fig. 18. For 2.842 nH and 0.123 pF, the DSS dimensions on the ground are determined to be d=4.8 mm and g=0.6 mm. It has been already proven that the inductance of 2.842 nH and the capacitance of 0.123 pF and its corresponding DSS dimensions (d=4.8 mm and g=0.6 mm) generate the same cutoff frequency of 4.2 GHz in Fig. 26. The parallel lumped capacitance of C_{p1} and C_{p3} can be easily realized for the distributed circuit model by using the transmission line theory in Fig. 29, where the characteristic impedance of the stub line is defined as 30 ohm. The parallel capacitances of C_{p1} and C_{p3} are calculated as 0.757 pF by using (50).

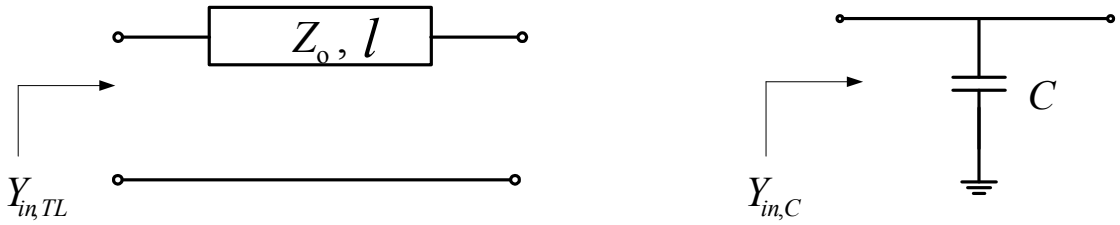

(a) (b)

Fig. 29. The equivalent circuit models of (a) a microstrip transmission line and (b) a lumped parallel capacitor.

The input admittance of each model, (a) and (b), in Fig. 29 is presented in (51) and (52). The equivalent distributed stub dimensions of this parallel capacitor in Fig. 29 (b) can be found by equating these two equations. Since the characteristic impedance of the shunt stub is already set at 30 ohm, the shunt stub width (w_s) can be calculated with the substrate information. For the parallel capacitance of 0.757 pF, the width and length of the microstrip stub are found to be w_s=4.7 mm and l=4.38 mm, respectively. Figure 30 represents the relation between the lumped and distributed model of a LPF with a DSS on the ground plane.

$$Y_{in,TL} = jY_o \tan(\beta \cdot l) \tag{51}$$

$$Y_{in,C} = j\omega C \tag{52}$$

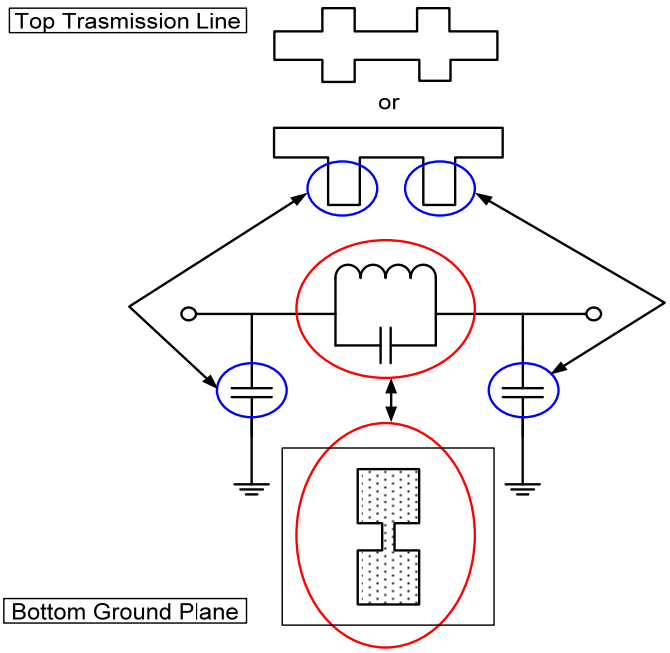

Fig. 30. The transformation from the lumped model of dumbbell shaped slot LPF to its distributed circuit model.

Figure 31 presents the circuit and EM simulated and measured results of the LPF with the dumbbell shaped slot designed with the conventional method. As it is shown, the circuit simulation demonstrates the 3 dB cutoff frequency of 4.2 GHz exactly, however the EM simulated and measured cutoff frequencies are shifted to the left by 1 GHz because of the increased inductance due to the shunt stub width. Thus, the conventional LPF design method with a dumbbell shaped slot faces the problem of limiting the parallel stub because the 3 dB cutoff frequency error increases as the number of stubs increase. One of the easiest ways to produce steep cutoff characteristics is to increase the number of parallel stub sections, but this is not suitable for the conventional design method. To overcome this, the additional inductance due to the

parallel stub sections should be subtracted from the inductance generated by a slot section, thus one could increase the number of element stages without the cutoff frequency error.

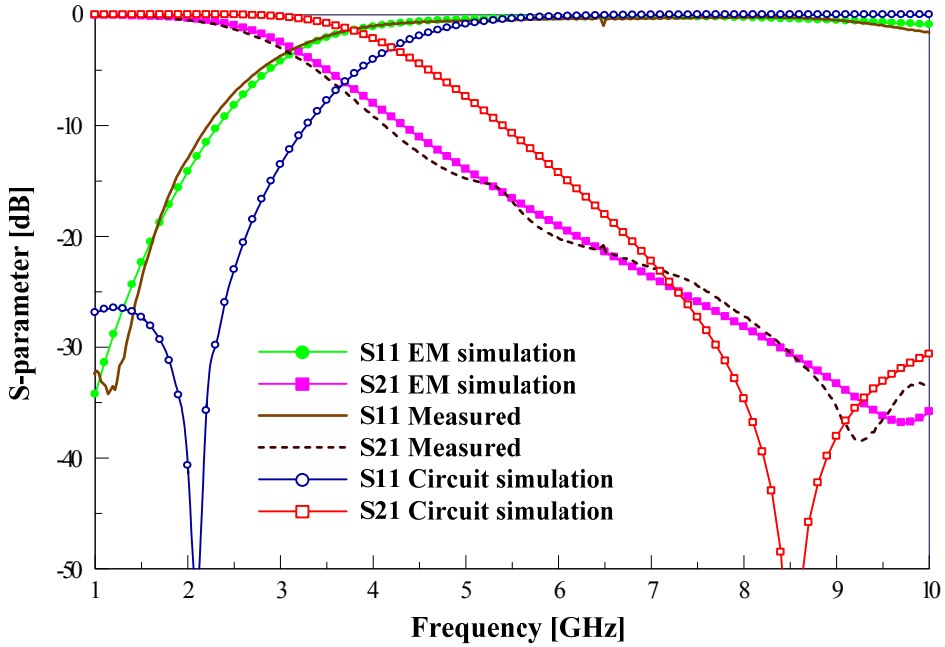

Fig. 31. The simulated and measured results by using the conventional LPF design method with a dumbbell shaped slot.

C. Proposed Lowpass Filter Design with DSS

Finding the exact inductance from the parallel stub sections is primarily required to design a LPF without cutoff frequency error. The proposed method starts with assuming that the undesirable inductance is added to an inductance produced by two square slot areas of a DSS. The following steps are used to attain the desired solution.

Step 1) π-type equivalent circuit of microstrip transmission line is investigated by using even and odd mode analysis. Image theory supports this step.

Step 2) A mathematical expression representing an inductance in the π-type equivalent circuit is derived. This expression is used to account for the parasitic inductance of parallel stub sections.

In this section, the static analysis of a transmission line is used, and its validity is confirmed by EM theory. By choosing two different excitation modes from the each end of a transmission line, the perfect magnetic conductor (PMC) or perfect electric conductor (PEC) can be virtually constructed in the middle of the microstrip transmission line. This satisfies the image theory that validates the static analysis method. Since the waves are incident from the sources placed at each end of the transmission line, the standing wave pattern is formed; this wave pattern still conserves a plane wave. Figure 32 shows the image theory illustrating the direction of two different current sources over the PEC and PMC boundaries. The normal component of an electric current source and its image component are in the same direction over a PEC boundary while they are in the opposite direction on a PMC surface [29].

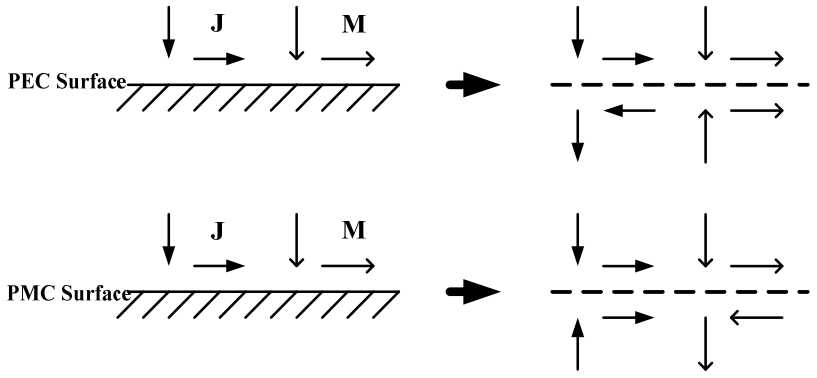

Fig. 32. The electric and magnetic current distributions on the PEC and PMC boundaries by image theory.

A microstrip transmission line cannot support a pure transverse electromagnetic (TEM) mode because of its unsymmetrical structure, but it could be considered as an approximate TEM wave structure in the low frequency range, where the strip width and substrate thickness are much smaller than the guided wavelength. Any two port network can be represented as a π or T network, thus the microstrip line can be modeled as a π or T network by considering the transmission line itself as a two port network. To find the parasitic inductance of the transmission line, an equivalent circuit of the microstrip is modeled as a π-network in Fig. 33. Since the fundamental propagation mode of a microstrip transmission line is assumed as a TEM mode, surface currents on a strip line can be expressed as (53).

$$\vec{J}_S = \hat{n} \times \vec{H}_S \tag{53}$$

In (53), the unit vector ($\hat{n}$) is in the normal direction to the strip surface.

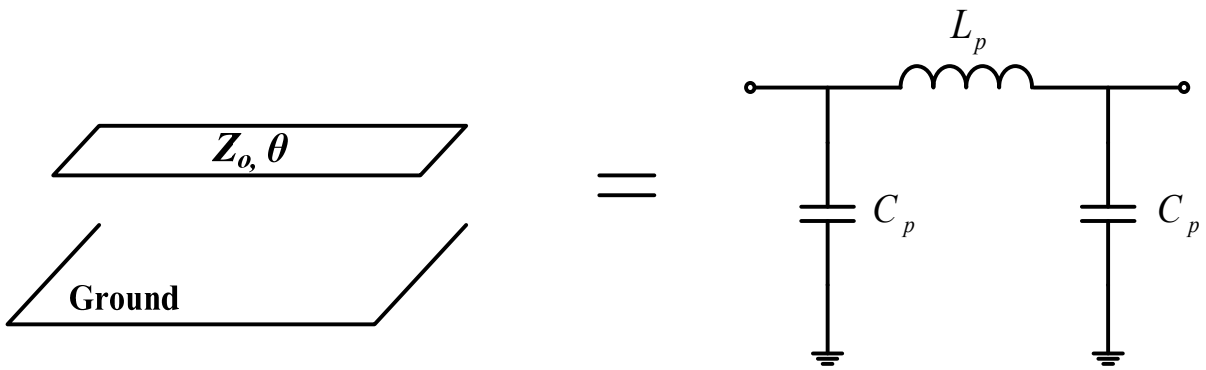

(a) (b)

Fig. 33. Equating (a) a microstrip transmission line and (b) a π-type lumped equivalent circuit model.

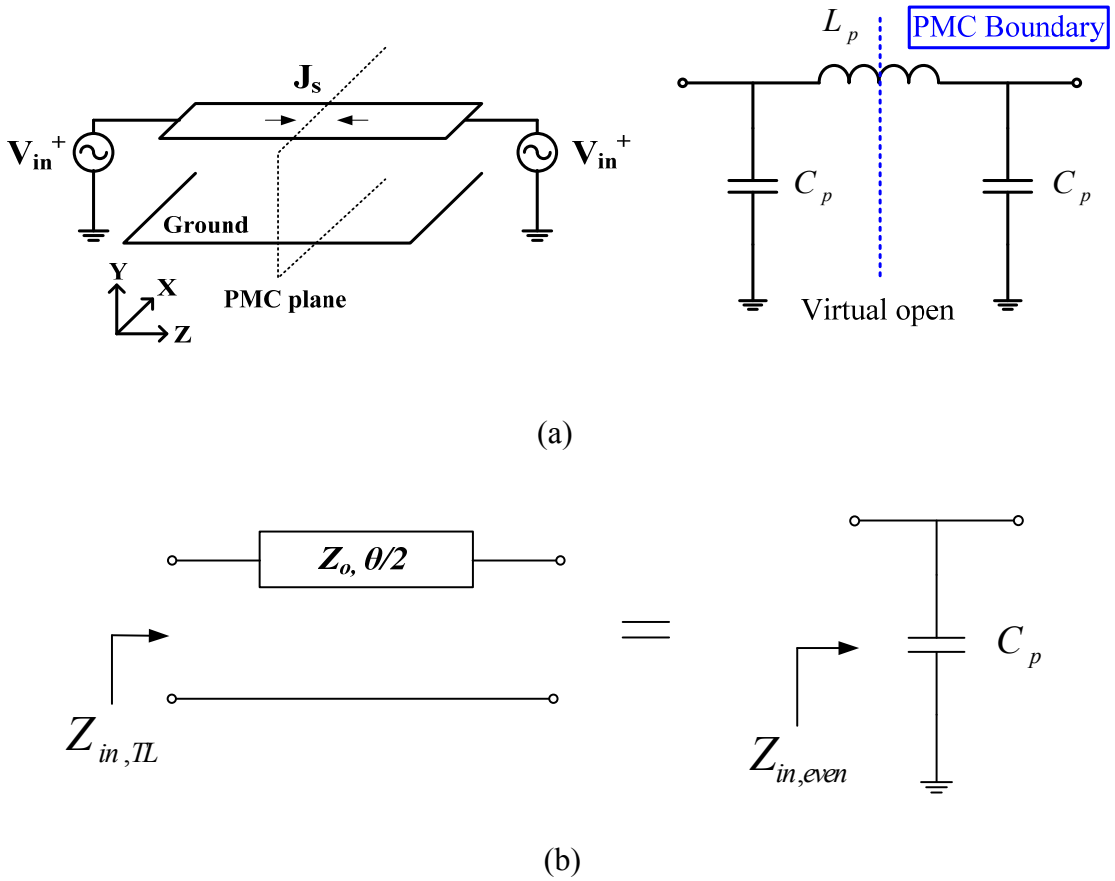

Fig. 34. π-type lumped equivalent circuit models for an even mode (a) the surface current distribution on a strip line, and (b) its resulting lumped equivalent circuit model for an even mode.

Figure 34 presents the microstrip transmission line with the symmetrical excitation and its lumped equivalent circuit for an even mode. For a symmetrical excitation the electric field must be a maximum on the cross section plane. Because the waves travel the same distance from the source, they are in phase and their magnitudes are added on the cross section plane. Thus, as one can see from (54), the electric field is a maximum when the magnitude of a voltage wave is a maximum.

$$\vec{E} = -\nabla V \tag{54}$$

From the standing wave pattern, the magnetic field is a minimum when the electric field is a maximum. Thus the cross section plane is shown as the PMC boundary according to the boundary condition. On that cross section plane the maximum tangential electric field is in the same direction and the normal surface current is in the opposite direction for a $\lambda_g/2$ period. This PMC plane makes a π-type equivalent circuit that is virtually open, as shown in Fig. 34 (a). Thus, the parallel capacitor in the left side is only activated in Fig. 34 (b). The input impedance of a microstrip line and its lumped equivalent circuit are shown in (55) and (56). These equations are derived from Fig. 34 (b).

$$Y_{in,TL} = \frac{1}{Z_{in,TL}} = jY_o \tan\left(\theta/2\right) \tag{55}$$

$$Y_{in,even} = \frac{1}{Z_{in,even}} = j\omega C_p \tag{56}$$

By equating (55) and (56) at $\omega = \omega_c$, the parallel capacitance of a π- network can be calculated by (57).

$$C_p = \frac{1}{Z_o \omega_c} \tan\left(\theta/2\right) \tag{57}$$

In general, this parasitic parallel capacitance is small enough so that one could ignore its effect for the low frequency band. The series inductor of a π- network is dominant for determining the cutoff frequency, so the series inductance, which increases

the overall inductance of the LPF, is the important parameter to design an accurate LPF with a dumbbell shaped slot.

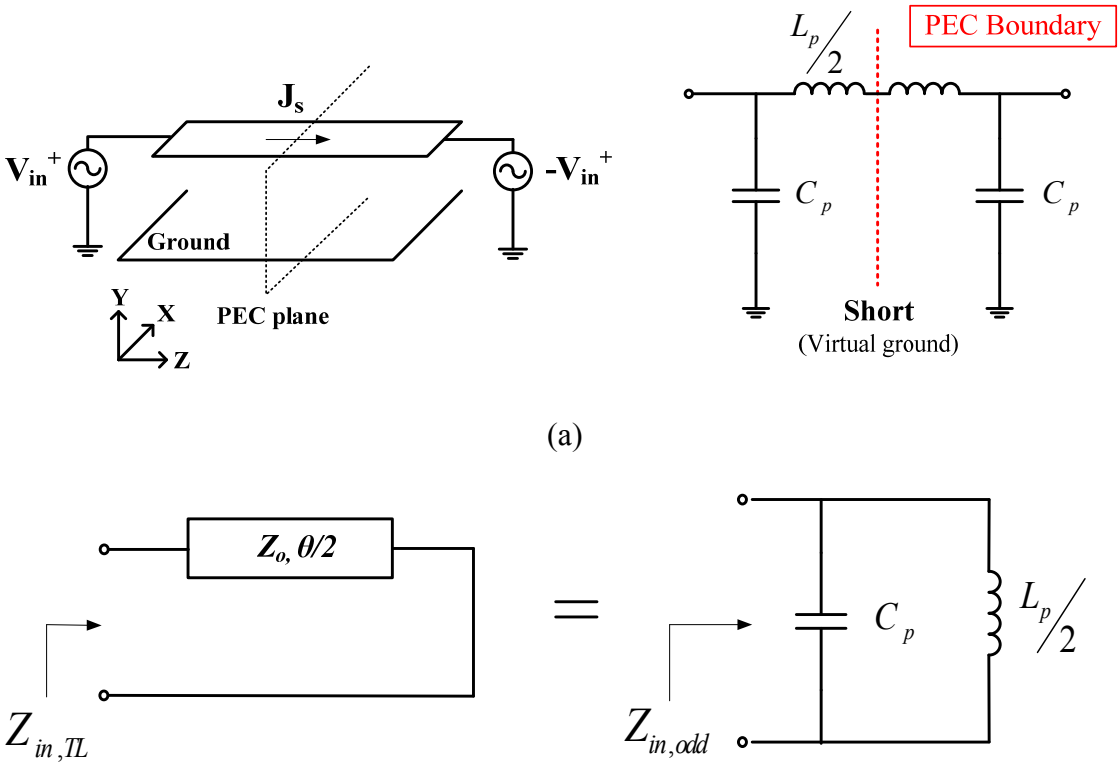

Fig. 35. π-type lumped equivalent circuit models for the odd mode (a) surface current distribution on the strip line, and (b) the resulting lumped equivalent circuit model for odd mode.

For an asymmetrical excitation the cross section plane appears as PEC boundary. Two different voltage waves with the same magnitude but opposite signs are subtracted on the cross section plane, thus the electric field is a minimum but the magnetic field is a

maximum. This field distribution can be also verified from the standing wave pattern. Since the tangential electric field is a minimum, this cross section plane is shown as a PEC boundary. This presents an odd mode equivalent circuit model of a π-network in Fig. 35. In this mode, a virtual short point is generated in the middle of the π-network equivalent circuit, so the resulting model is illustrated in Fig. 35 (b). For an odd mode case, the input impedance of a microstrip line and its lumped equivalent circuit are shown in (58) and (59). These equations are derived from Fig. 35 (b).

$$Y_{in,TL} = \frac{1}{Z_{in,TL}} = -jY_o \cot\left(\frac{\theta}{2}\right) \tag{58}$$

$$Y_{in,odd} = \frac{1}{Z_{in,odd}} = j\left(\omega C_p - 2/\omega L_p\right) \tag{59}$$

By equating (58) and (59) at $\omega = \omega_c$, the equation for a series inductance can be derived. In (59), C_p is the same as (57). Equation (60) presents the series parasitic inductance due to a shunt stub section, and Z_o is the characteristic impedance of the stub line.

$$L_p = \frac{Z_o}{\omega_c} \sin\theta \tag{60}$$

This parasitic inductance is generated by the line width of the shunt stub. A wider shunt stub width produces a bigger parasitic inductance because of the increased wave travel distance. As a result, the increased overall inductance lowers the actual 3 dB cutoff frequency point compared to their circuit simulation. Since this parasitic inductance is added to the inductance caused by the DSS dimensions, it should be subtracted from the total inductance of a DSS to keep the desired cutoff frequency of a LPF. The modified

inductance equation from (48) is presented in (61) where Z_o^s is defined as the characteristic impedance of the parallel stub, and θ is shown in (62).

$$L_{DSS} = \frac{3}{4\omega_c}(g_1 \cdot Z_o) - 2 \cdot \frac{Z_o^s}{\omega_c} \sin\theta \tag{61}$$

$$\theta = \beta \cdot w_s = \frac{2\pi}{\lambda_{g,cutoff}} \cdot w_s = \frac{2\pi}{\lambda_{o,cutoff}} \cdot \sqrt{\varepsilon_{eff}} \cdot w_s \tag{62}$$

To calculate the parasitic inductance from the shunt stub width, the effective dielectric constant (ε_{eff}) should be known. The parameters w_s and ε_{eff} in (62) are defined as the shunt stub width and the effective dielectric constant, respectively, for the characteristic impedance of the parallel stub (30 ohm). Figure 36 shows the parameters w_s and Z_o of the parallel stub. Since the width of the shunt stub is already determined as w_s=4.7 mm, its corresponding inductance can be calculated by (60). With a substrate thickness of 0.762 mm, a dielectric constant of 2.2, and a characteristic impedance of 30 ohm, ε_{eff} is found to be 1.95 [30], and θ is determined as θ =33° from (62). Finally, the parasitic inductance (1.23 nH) caused by the two parallel stub lines is counted with the inductance (2.84 nH) from a DSS dimension. As a result, the new L_{DSS} is calculated as 1.61 nH by the modified inductance equation in (61).

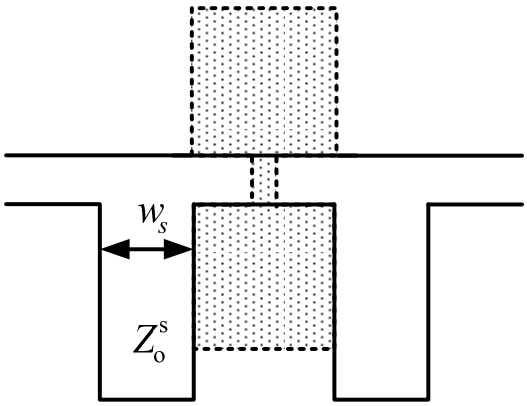

Fig. 36. The parameters (w_s and Z_o) of a parallel stub causing parasitic inductance.

The new DSS slot dimensions producing the inductance of 1.61 nH can be immediately found as d=3.3 mm by the inductance curve-fitting graph in Fig. 18. Figure 37 shows the photos of this fabricated LPF. Figure 38 compares the results of circuit simulation, EM simulation, and measurement. The simulated and measured results show the exact 3 dB cutoff frequency at 4.2 GHz. Thus, any additional tuning work to meet a desired cutoff frequency is not required with this proposed design method.

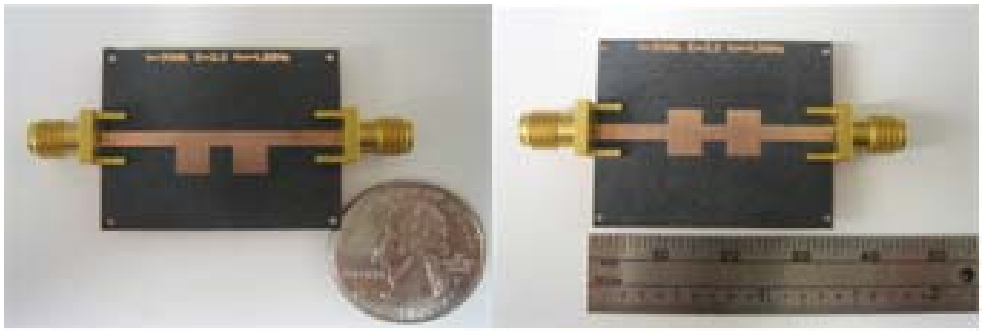

(a)

Fig. 37. The fabricated LPF with a single DSS on the ground plane (a) The top and (b) the bottom view.

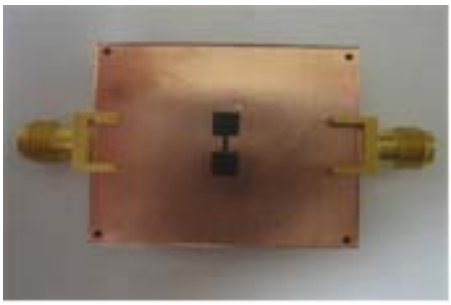

(b)

Fig. 37. Continued.

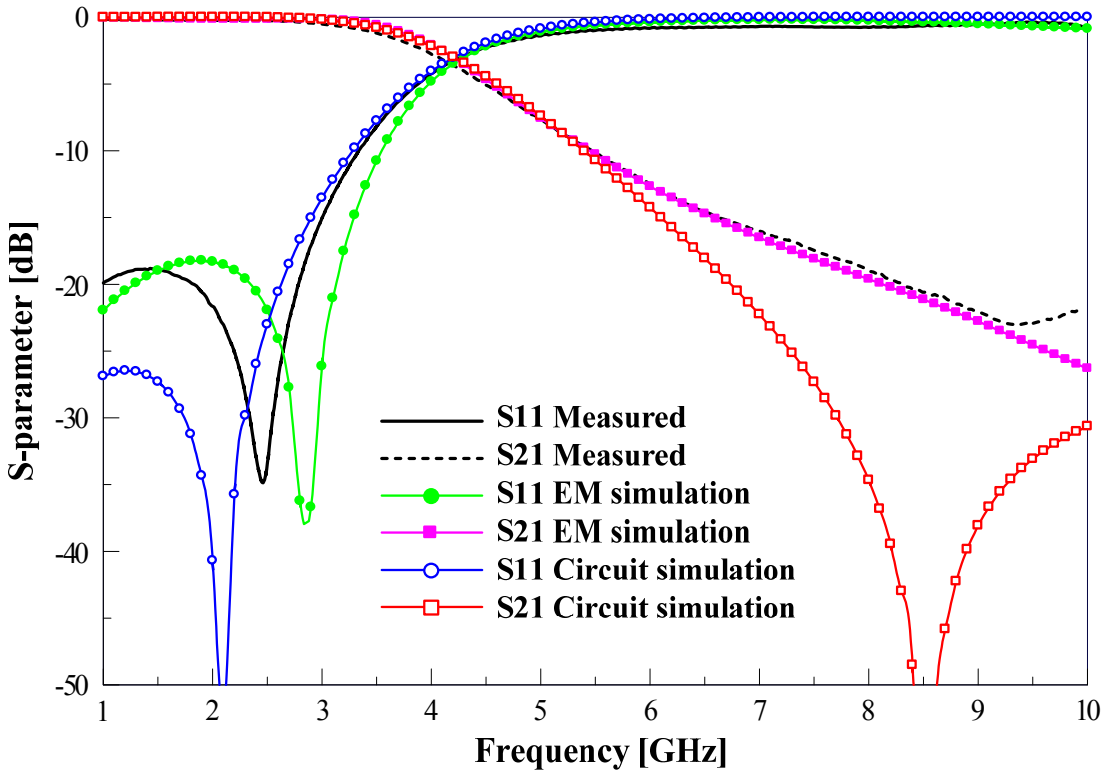

Fig. 38. Simulated and measured results by using the proposed LPF design method with a dumbbell shaped slot.

D. Conclusions

In this chapter, an accurate analysis and design technique for a LPF with a dumbbell shaped slot have been introduced. An equivalent circuit extracting method for a single DSS is based on an insertion loss type filter design theory. The validity of the equivalent circuit extracting method is proven by circuit simulation and electromagnetic field analysis. Inductance and capacitance curve fitting graphs that depend on the slot dimensions are also plotted and used to define the dimensions of a DSS on the ground. Two LPFs designed by using conventional and proposed methods are compared to one another. The insertion loss in the pass-band is measured as less than 0.2 dB from both LPFs. The simulated and measured results prove the validity of the proposed method.

CHAPTER VI

UWB BANDPASS FILTER DESIGN WITH GROUND SLOTS

A. UWB Bandpass Filter Design on Microstrip

Recently, the ultra-wideband (UWB) radio system design techniques have been attracted by many researchers and engineers from both in academy and industry since the Federal Communications Commission (FCC) has released the frequency band from 3.1 GHz to 10.6 GHz for commercial applications in 2002 [31]. Filters with wide pass-band, sharp frequency cutoff characteristics, and flat group delay are required for broadband communication systems. For these reasons, vigorous researches have been conducted and numerous results have been reported [32]-[34]. The basic principle of a broadband pass filter is to generate the multi resonant poles to produce wide pass-band and this can be realized by tight coupling between resonators. However, increasing the coupling may cause the low Q-factor and thus high insertion loss.

In this section, the UWB band-pass filter with ground slots introduced in [34] is studied, simulated, and measured. Furthermore, based on its theory in [34], UWB band-pass filter is designed with coplanar waveguide (CPW) structure.

Most of fields in microstrip transmission line is confined between the top strip line and bottom ground. By placing a slot underneath the parallel coupled line, the coupling between two parallel strip lines can be increased. The inductance is also produced by the ground slot underneath the gap because the gap disturbs the current flows on the ground

plane. Figures 39 and 40 show the UWB band-pass filter configuration on microstrip with slots on the ground plane.

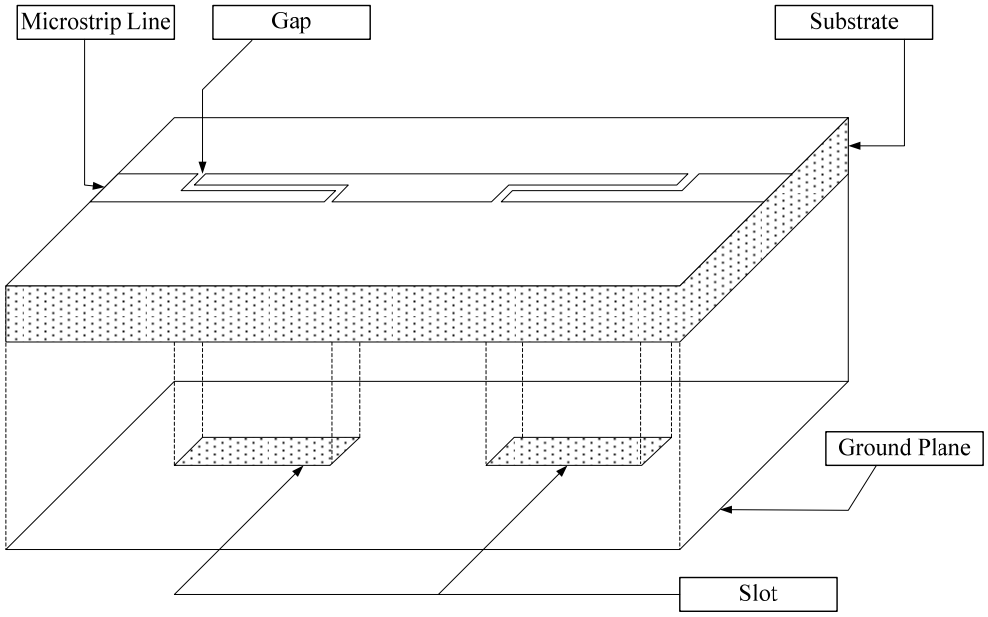

Fig. 39. UWB bandpass filter circuit configuration with two square slots on the ground.

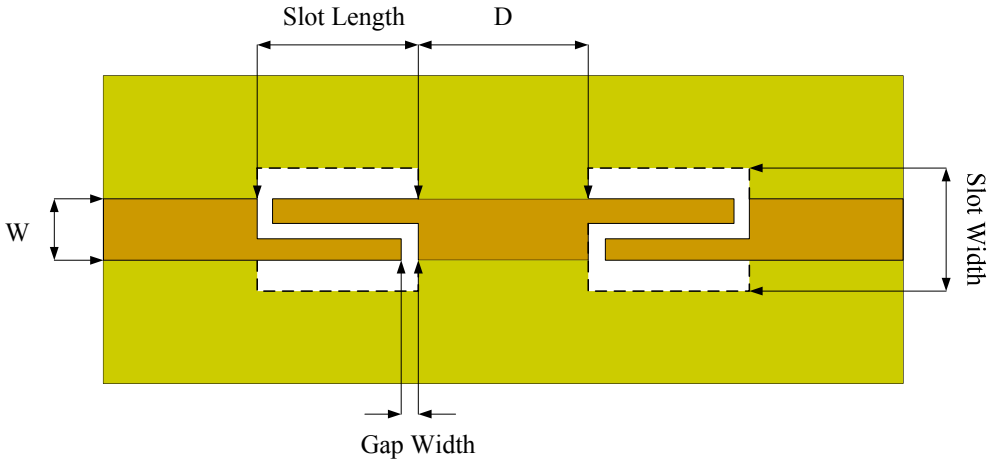

Fig. 40. Parameters of UWB band-pass filter with two square slots on the ground.

To study the resonant characteristic of a parallel line gap, EM simulation using finite element method (FEM) is conducted through HFSS [27]. As the slot length in Fig. 40 varies with different dimensions, gap width is fixed. When the dimensions of the gap width changes, slot length is fixed. Frequency response with the varying slot length dimensions is shown in Fig. 41. By increasing the slot length, the upper cutoff frequency is dramatically decreased compared to the lower cutoff frequency. Increasing the slot length generates the additional inductance since the length of the thin line of coupling gap becomes longer. Therefore, the inductance is more dominant to upper cutoff frequency. Figure 42 shows the frequency response as the gap width varies with different dimensions. As the gap width increases, the gap capacitance decreases. Decreased gap capacitance is more dominant to lower cutoff frequency. Thus, by changing the slot length and gap width, the upper and lower cutoff frequency can be adjusted.

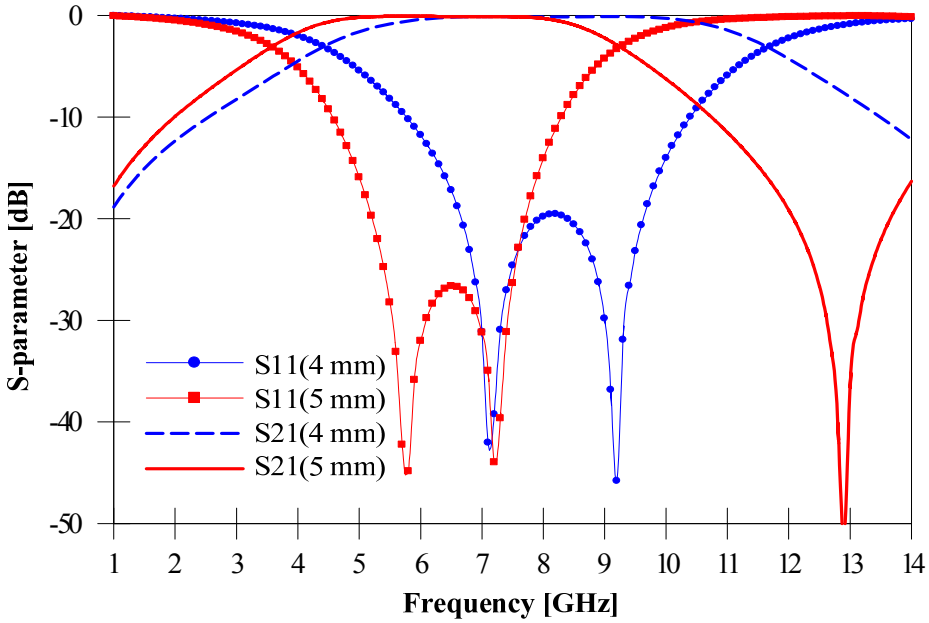

Fig. 41. Slot length variation (gap width fixed as 0.3mm).

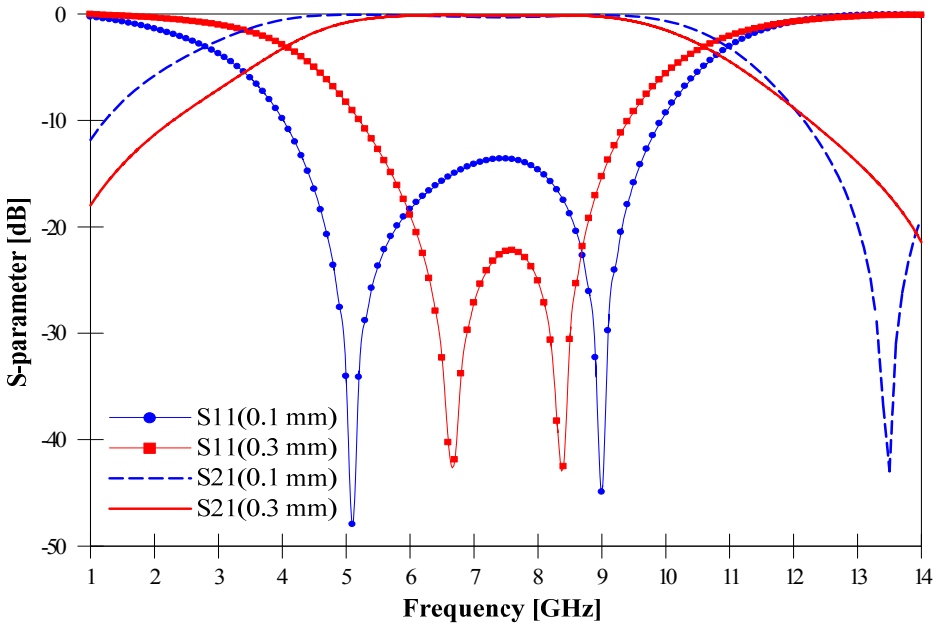

Fig. 42 Gap width variations (slot length fixed as 4.4mm).

UWB band-pass filter is designed with the dimensions of slot length=4.4 mm, gap width=0.1 mm, slot width=2.3 mm, D=7.7 mm, and W=0.6 mm. Figure 43 shows the photos of a fabricated circuit and Fig. 44 presents the simulated and measured results of the UWB band-pass filter with those dimensions.

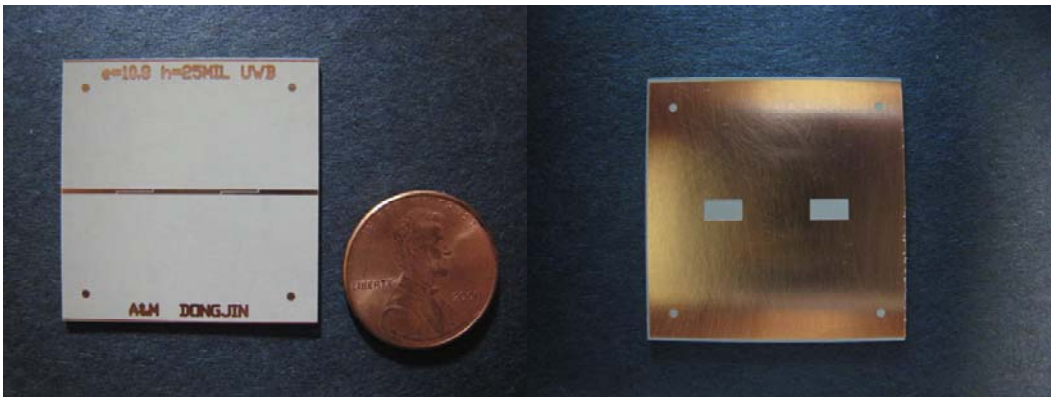

(a) (b)

Fig. 43. Image of fabricated UWB band-pass filter on microstrip.

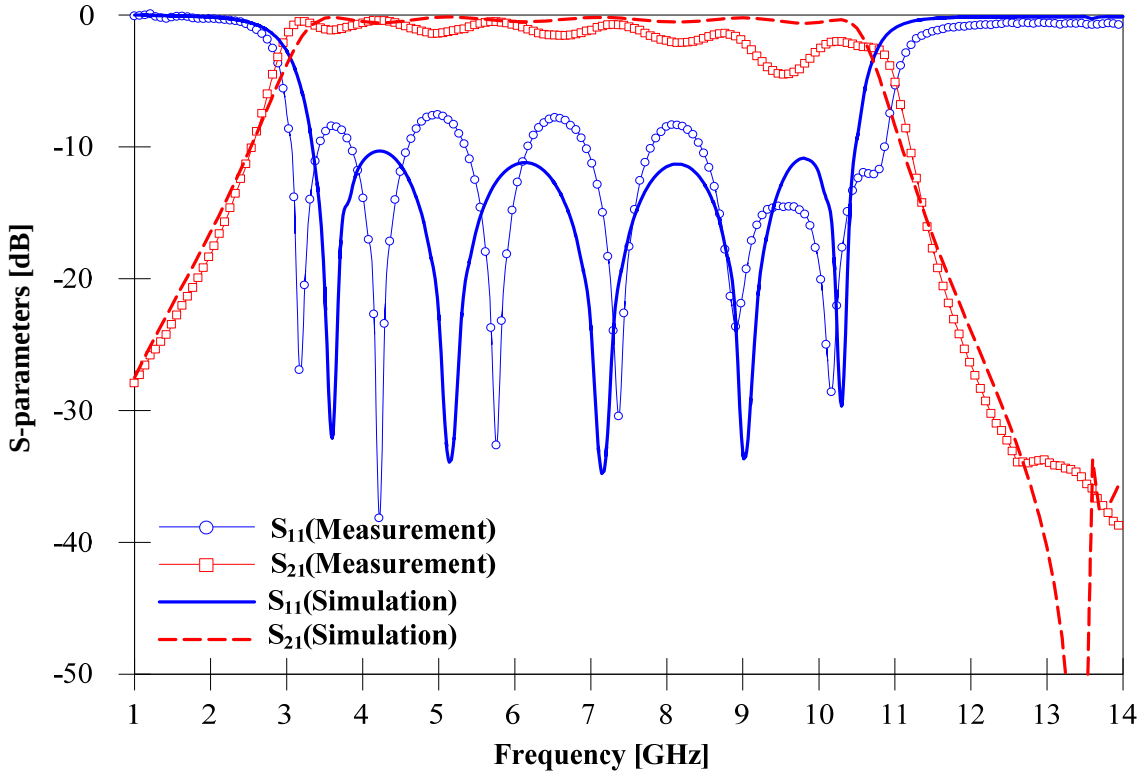

Fig. 44 Simulated and measured UWB band-pass filter.

B. UWB Bandpass Filter Design on Coplanar Waveguide

Many commercial RF/microwave applications have been appeared since microwave monolithic integrated circuit (MMIC) techniques had been introduced. Compared to hybrid type circuits, MMICs have advantages such as compact size, light weight, and low production cost for mass production. For some applications, CPW type circuits have advantages for MMIC designs because solid-state devices can be easily mounted. Thus, UWB filter design using CPW is needed for these applications.

Coplanar waveguide was first introduced by Wen [35] in 1969. The electric and magnetic field distributions of even and odd mode for CPW transmission line are shown in Fig. 45. Even mode, so called coplanar waveguide mode, is a quasi-transverse electromagnetic (qusi-TEM) mode with even symmetry to the vertical plane A-A' and its dispersion is very low [36]. Because of the low dispersion characteristic of the even mode, broadband applications are possible with this mode. In other hands, odd mode, so called slot line mode, has opposite signs for each side ground plane. Since the potentials are different for two ground planes, the electric field lines are headed from one to the other. Magnetic fields are in longitudinal direction and this odd mode has competitively large dispersion effect. The parameters for CPW cross section are shown in Fig. 46.

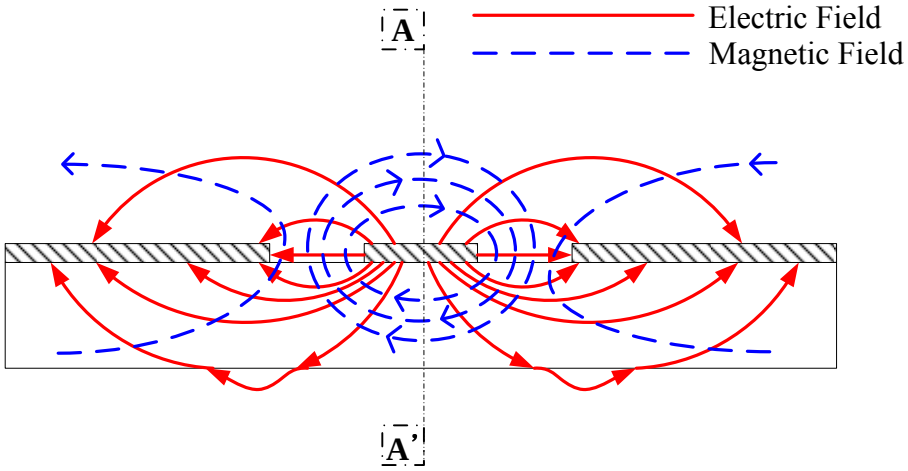

(a)

Fig. 45. Electric and magnetic field distributions of the (a) even mode and (b) odd mode on a CPW.

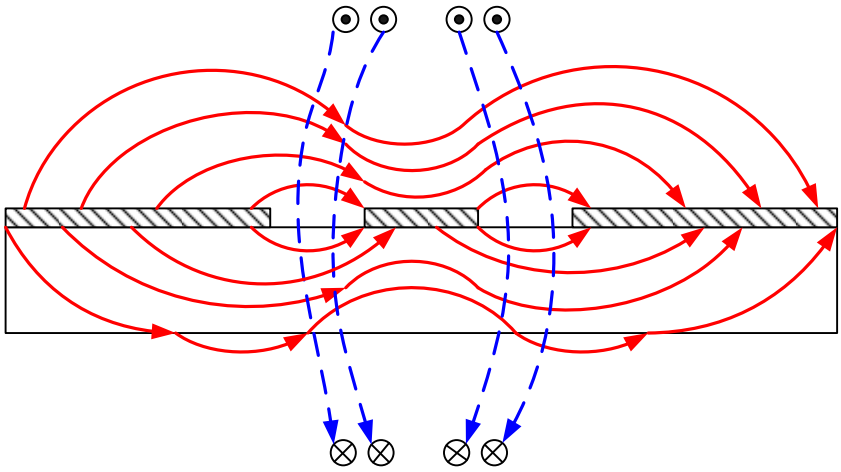

(b)

Fig. 45. Continued.

Wen [35] has carried out a quasi-static analysis of these transmission lines using conformal mapping and with the assumption that the dielectric substrate is thick enough to be considered infinite [37]. This conformal mapping method is an analytical analysis and gives the exact solution. In this section, each derivation step is not introduced, but some fundamental equations are shown for CPW transmission line analysis.

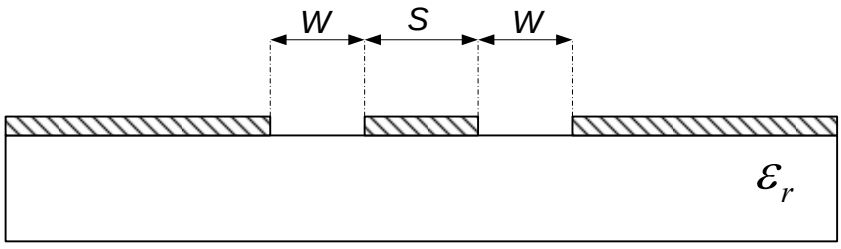

Fig. 46. Cross section of CPW transmission line.

Equations (63)-(68) are found in [38]. These equations are useful for determining the characteristic impedance of CPW transmission line. Here the $K(k)$ is the complete elliptical integral of the first kind. The parameters, k and k', are the elliptic modulus of an elliptic integral and the complementary modulus, respectively. Complete elliptic integrals with respect to the complementary modulus are also denoted as $K'(k) = K(k')$ [38]. The characteristic impedance, Z_c, and effective dielectric constant, ε_{eff}, are given below in (63) and (64).

$$Z_c = \frac{\sqrt{\mu_o / \varepsilon_o}}{4 \cdot \sqrt{\varepsilon_{eff}}} \cdot \frac{K(k')}{K(k)} \tag{63}$$

$$\varepsilon_{eff} = \frac{1}{2}(1 + \varepsilon_r) \tag{64}$$

where

$$\frac{K(k)}{K(k')} = \frac{1}{\pi} \cdot \ln\left(2\frac{1+\sqrt{k}}{1-\sqrt{k}}\right) \text{ for } 0.7 \le k < 1 \tag{65}$$

$$\frac{K(k)}{K(k')} = \frac{1}{\pi} \cdot \ln\left(2\frac{1+\sqrt{k'}}{1-\sqrt{k'}}\right)^{-1} \text{ for } 0 < k \le 0.7 \tag{66}$$

$$k = \frac{S}{S + 2W} \tag{67}$$

$$k' = \sqrt{1 - k^2} \tag{68}$$

Based on the techniques in previous section, the two grounds on each side of parallel coupling gap have slots to produce the tight coupling between two parallel coupled lines in Fig. 47. Figure 48 shows the photo of the fabricated UWB bandpass filter on CPW.

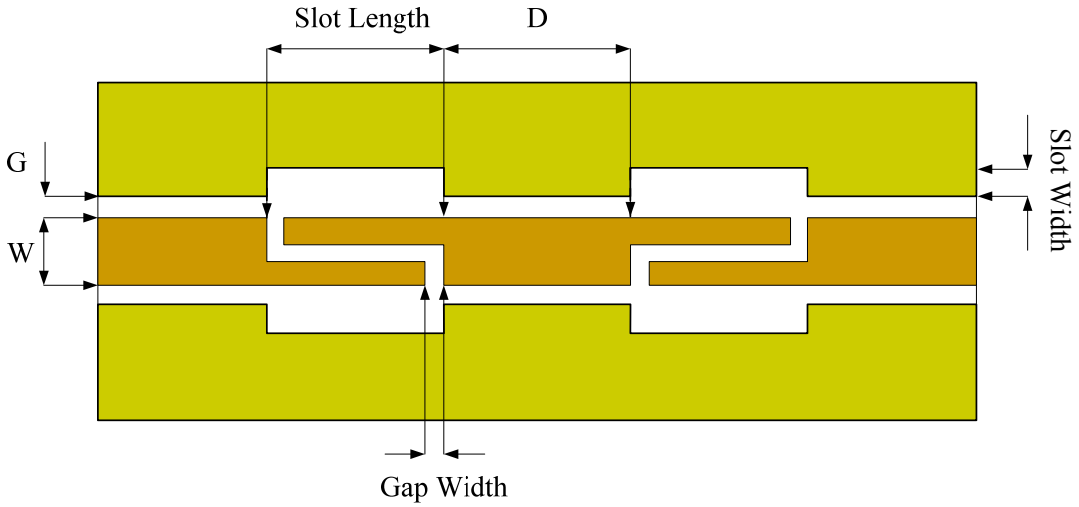

Fig. 47. UWB band-pass filter with two square slots on CPW.

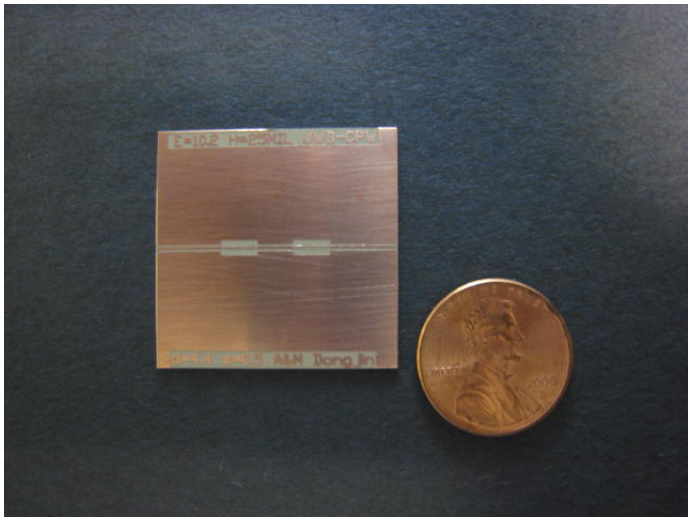

Fig. 48. Image of the fabricated UWB bandpass filter on CPW.

UWB band-pass filter is constructed on CPW and its dimensions are given in the following: slot length=4.4 mm, gap width=0.1 mm, slot width=0.5 mm, W=0.37 mm, G=0.2 mm, and D=5 mm. Figure 49 present the simulated and measured results of this filter.

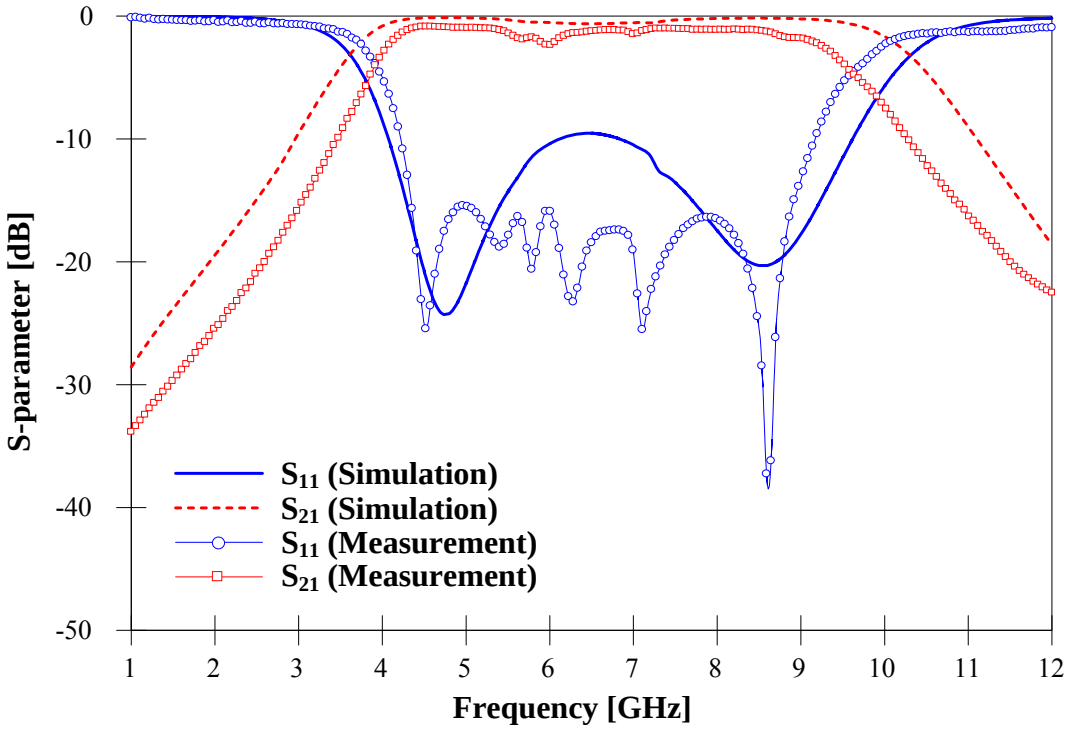

Fig. 49 Simulated and measured UWB band-pass filter in CPW.

CHAPTER VII

RECTENNA DESIGN USING LOWPASS FILTER WITH DUMBBELL SHAPED SLOT

A. Rectenna Operation Theory

The term rectenna represents the rectifying antenna which converts microwave power to DC power. Basically, the rectenna includes the rectifying circuit as well as antenna. The rectification of microwave beam through a solid state device has studied by R. H. George in Purdue University [39]. Since this first study many researchers have investigated those techniques to increase the conversion efficiency [40]-[42].

Fig. 50 shows a block diagram of a rectenna. The source power is received by antenna and the source resistance (R_S) represents the input impedance of the antenna [43]. The main purpose of LPF between the antenna and rectifying circuit is to reflect harmonics generated by the rectifying diode. Thus the conversion efficiency of the rectifying circuit can be increased since the reflected harmonics by the LPF are re-rectified through the diode.

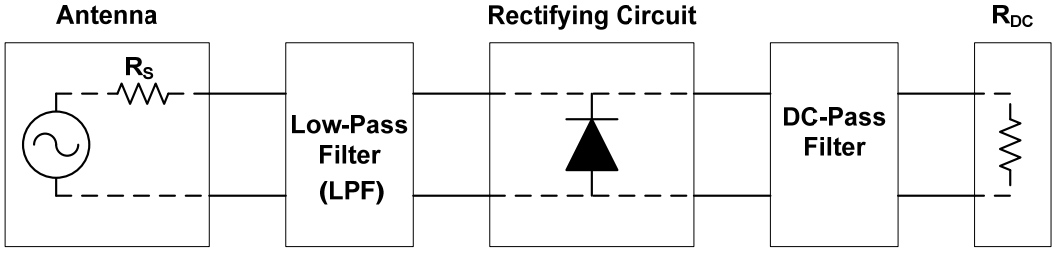

Fig. 50. Block diagram of rectenna circuit [43].

B. Comparison of Conventional and Simplified Rectenna

In this section, a 2.45 GHz rectenna using the conventional LPF with several parallel stubs is modified to reduce the rectenna dimensions. The LPF with a DSS is used to replace the conventional stub type LPF. By using the LPF with a DSS, the overall dimensions of the rectenna can be reduced. Generally, LPF with DSS has the advantage of reducing the harmonics as compared to conventional LPF with stubs.

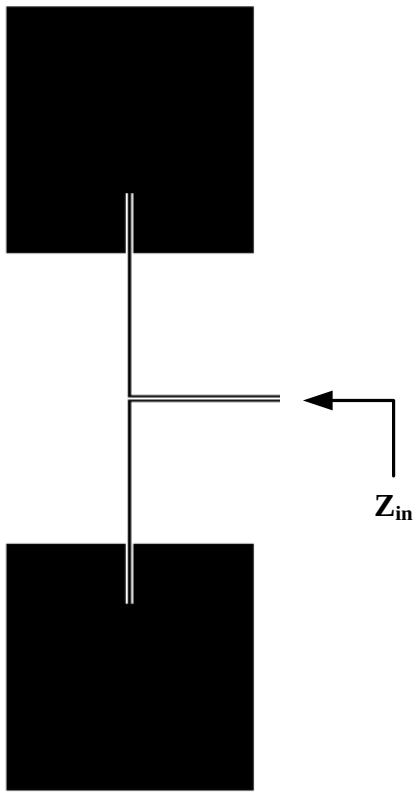

Fig. 51 Antenna design with transition from microstrip to CPS.

Figure 51 shows the antenna with transition from microstrip to coplanar strip line (CPS). By using CPS transmission line, the rectifying diode and lumped load resister can be easily mounted between the CPS transmission lines. Antenna's input impedance (Z_{in}) is found as 140 ohm by computer aided simulation using method of momentum (MoM). In rectenna design, antenna's input impedance is not necessary to match 50 ohm, but the input impedance of the location, where the rectifying diode is mounted, must be optimized for the conversion efficiency. This means that impedance matching is required between the rectifying diode and circuit. Approximately, allowable input impedance for mounting the diode is from 100 to 200 ohms. A M/A-COM's GaAs schottky barrier diode (MA4E1317) is used for rectification. The substrate used for fabrication has a thickness of h=30 mil and dielectric constant of ε=2.2. The line widths of the microstrip feed line and CPS are 0.4 mm and 0.2 mm, respectively.

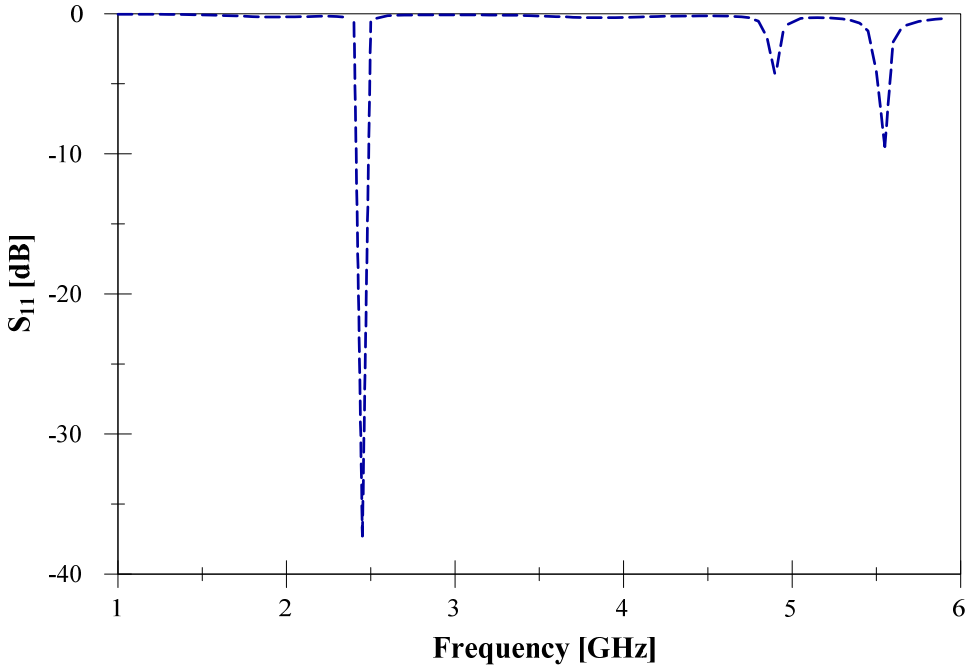

Fig. 52. The S_{11} characteristic of the antenna without LPF.

As shown in Fig. 52, the 2nd harmonic could be radiated at 4.9 GHz. The RF power at this frequency can be re-radiated through the antenna if no LPF is used. By placing a LPF this harmonic can be removed. Figure 53 represent the comparison of the conventional and modified rectenna model. By using LPF with DSS, overall rectenna dimensions can be reduced. Thus, this single rectenna using LPF with DSS can be used for array and the array dimensions can be also reduced. The block diagrams for Fig. 53 are shown in Fig. 54. The DSS used for this LPF is designed under the transmission line with the characteristic impedance of 100 ohm.

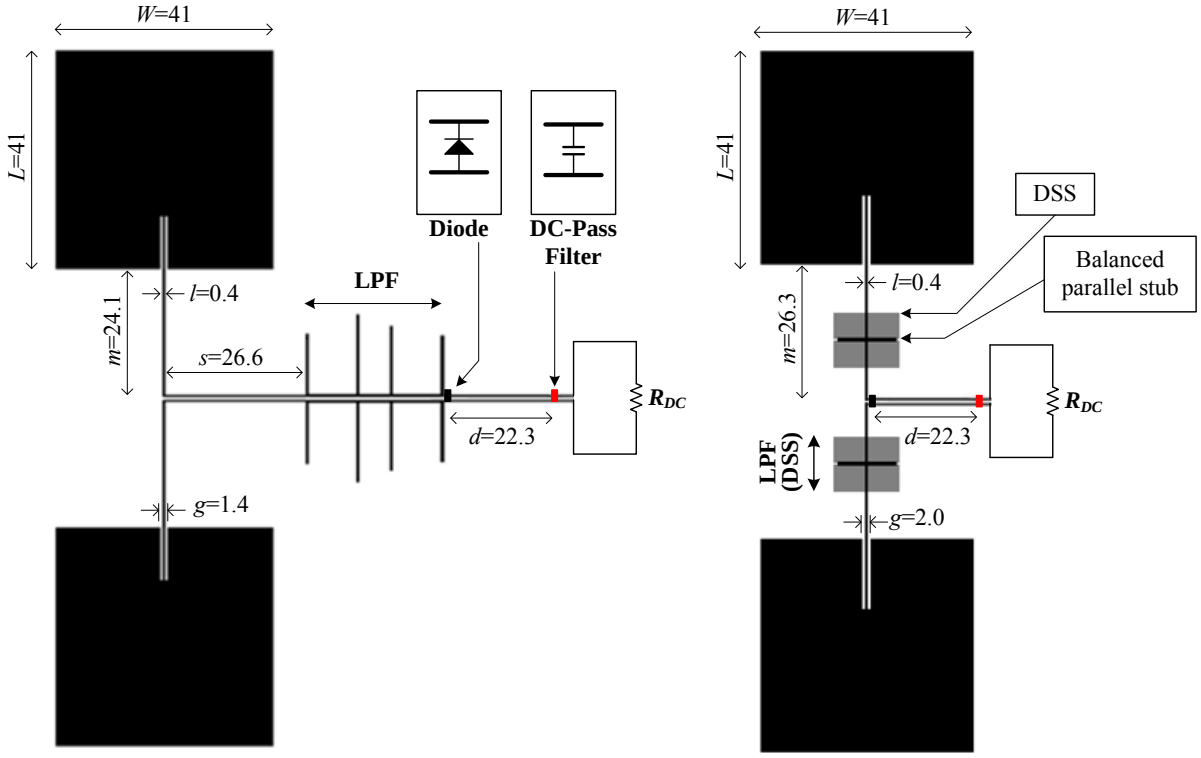

(a) (b)

Fig. 53. The 2.45 GHz rectenna comparison; (a) the conventional rectenna and (b) modified rectenna (dimensions are in mm).

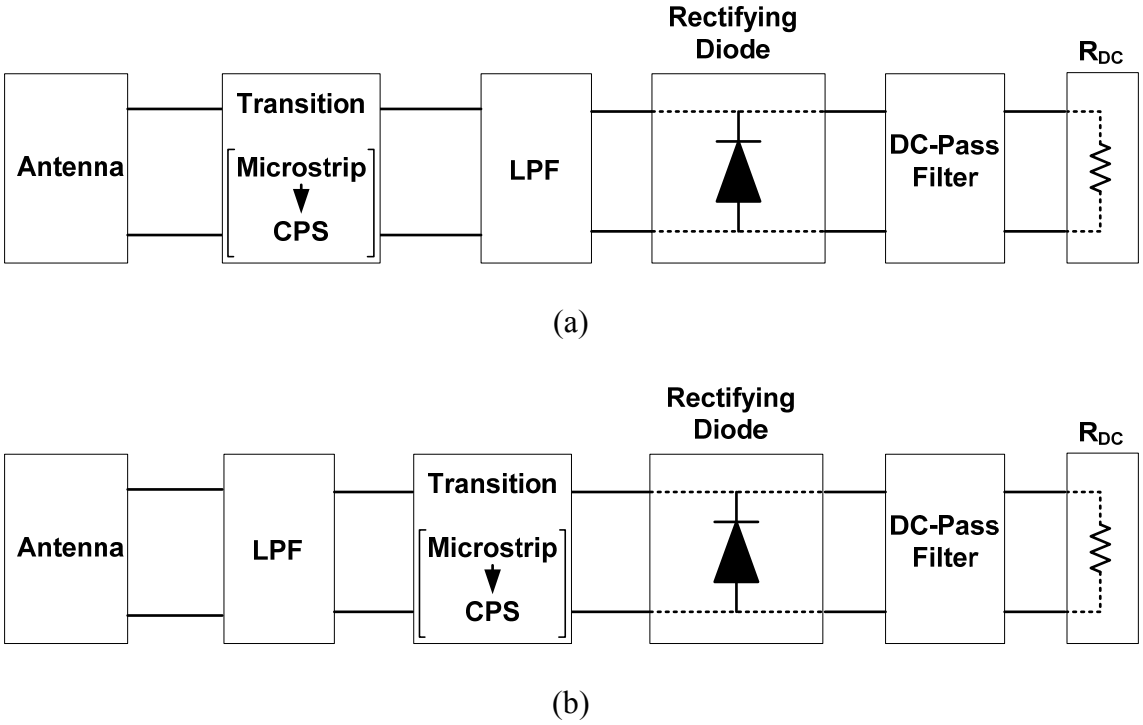

Fig. 54. The block diagrams of (a) the conventional and (b) modified rectenna.

C. Simulation and Measurement of Modified Rectenna

As shown in Fig. 55, the 2nd harmonic near 5 GHz can be removed by using a LPF. Thus, the most dominant second harmonic generated by the rectifying diode is trapped between the LPF and DC pass filter, i.e., capacitor. This trapped second harmonic is also converted to DC power through the rectifying diode. Therefore, the rectenna's conversion efficiency is increased by rectifying both fundamental (2.45 GHz) and second harmonic (4.9 GHz) RF power. Figure 56 shows the simulated unit rectenna array's radiation pattern through MoM and Fig. 57 presents the fabricated unit rectenna array. Transition from CPS to microstrip is used for measurement in Fig. 57. The rectenna is measured in the anechoic chamber of Electromagnetics and Microwave

Laboratory at Texas A&M University. Conversion efficiency of this unit rectenna array is determined by (70).

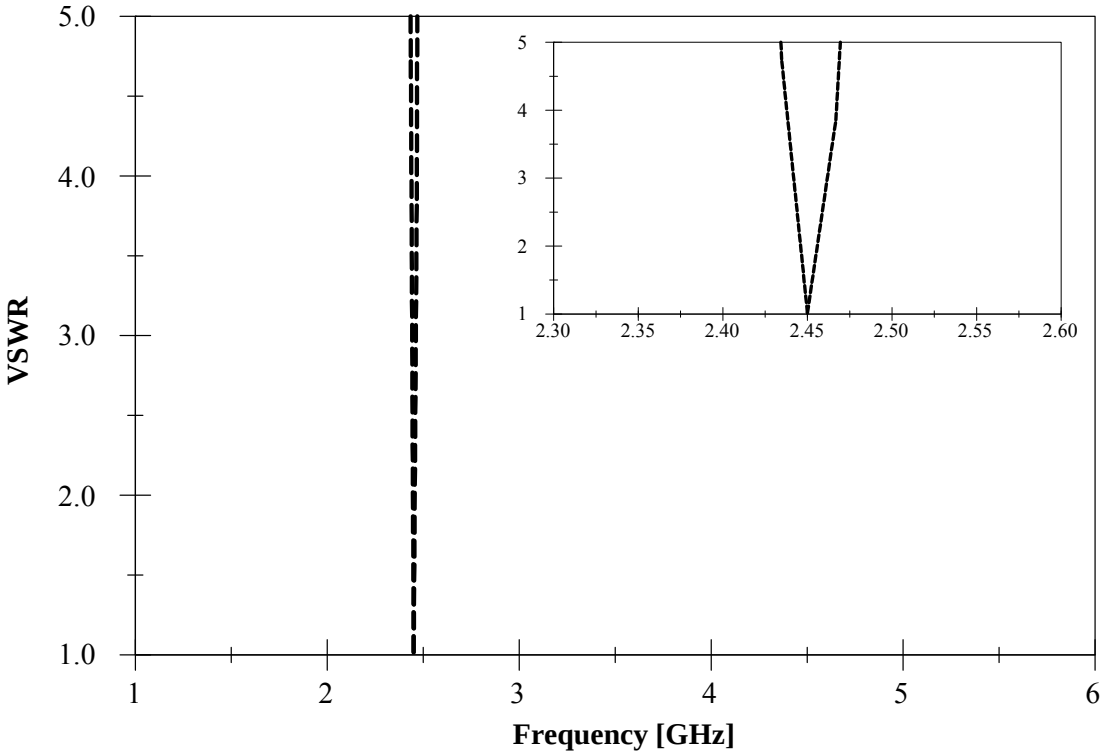

Fig. 55. Simulated VSWR of the rectenna with DSS-LPF.

$$P_{DC} = \frac{V_{DC}^2}{R_{DC}} \tag{69}$$

$$\eta_c = \frac{DC \text{ output power}}{RF \text{ input power received by antenna}} \times 100\ (\%) = \frac{P_{DC}}{P_{RF}} \times 100\ (\%) \tag{70}$$

P_{DC} (DC output power) in (70) is defined as (69). R_{DC} is the load resistance and V_{DC} is a measured voltage from rectenna. P_{RF} can be calculated from the Friis transmission equation. Parameters for calculating P_{RF} of the proposed unit rectenna array are shown in

Table 4. A standard gain horn antenna (Narda 644) is used for wireless RF power transmission. The rectenna's conversion efficiency depends on the electrical parameters of the rectifying diode and losses of microwave circuits at the operation frequency. In that sense, LPF for a rectenna must have low insertion loss. Measured insertion loss of the DSS-LPF used for this rectenna is less than 0.2 dB in pass-band.

Table 4. Parameters for the unit rectenna array

Frequency	λ_0 (cm)	Far field (cm)	G_r (dBi)	G_t (dBi)	A_e(cm^2)
2.45 GHz	12.2	87.1	8.0	14.5	74.5

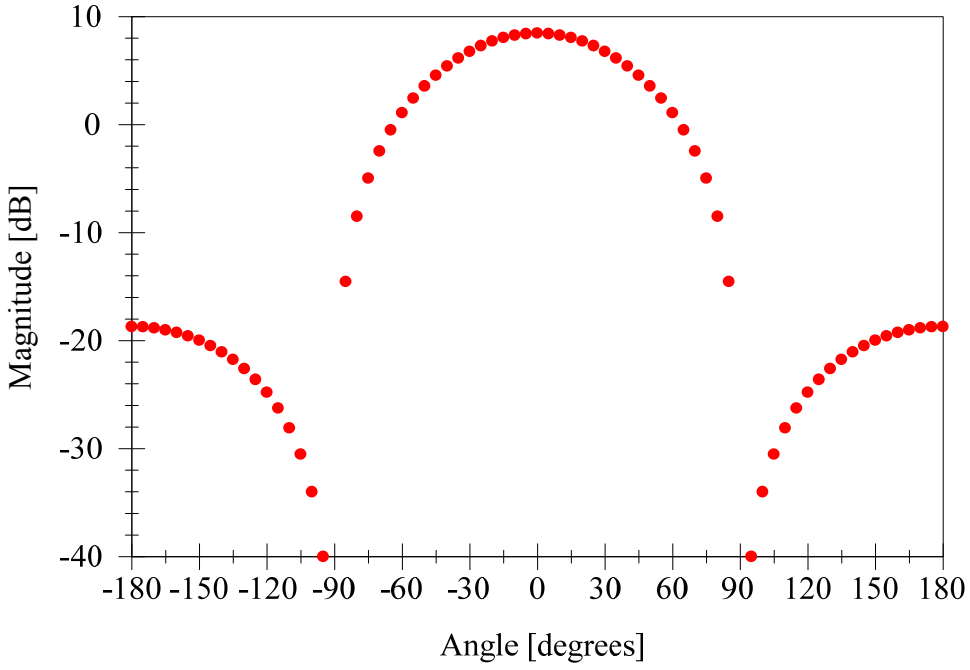

Fig. 56. Simulated rectenna's radiation pattern.

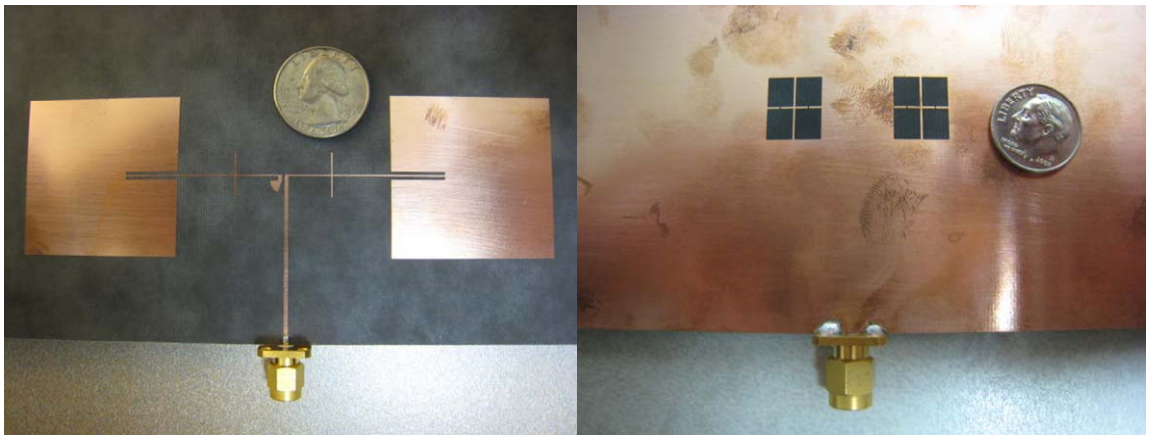

(a) (b)

Fig. 57. Modified rectenna in (a) top and (b) bottom view.

Measured rectenna conversion efficiencies are presented in Fig. 58. Maximum efficiency of 80.1 % is achieved at power density of 1.2 mW/cm^2 with the load resistance of 168 Ω.

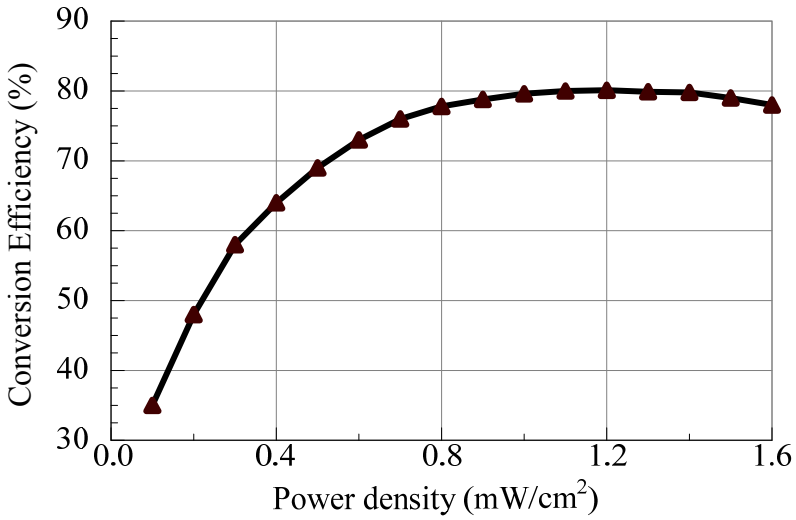

Fig. 58. Measured conversion efficiency.

CHAPTER VIII

CONCLUSIONS

A. Summary

In Chapters II and III, LPF design theory by insertion loss method is presented as background. By using this filter design theory, a dumbbell shaped slot (DSS) on the ground is analyzed and mathematical expressions are derived. Lumped equivalent circuit model of the dumbbell shaped slot (DSS) is presented and its validity is demonstrated through the comparison of circuit simulations, EM simulations, and measurements. Curve fitting analysis, which is for an inductance and capacitance versus a dumbbell shaped slot (DSS) dimensions, is also shown.

In Chapter IV, a periodic structure with dumbbell shaped slot on the ground is studied. Since the periodic structure provides both pass and stop bands, it can be treated as a filter. Equivalent circuit model of the proposed periodic structure is presented and analyzed by using cascaded network and transmission line theories. By placing the periodic slotted ground section in the ground plane, the characteristic capacitance and inductance of transmission line are changed. Therefore, the variations of these capacitance and inductance of transmission line also modify the propagation constant (β). The *k- β diagram* are plotted to estimate the pass/stop bands of this dumbbell shaped periodic structure. To validate the theory, a dumbbell shaped slot periodic structure with N=7 is fabricated and measured. Finally, the experimental results are compared with the calculated results and good agreement has been achieved.

In Chapter V, the LPF design using dumbbell shaped slot (DSS) is presented based on the previous studies in Chapters II and III. In this chapter, a new design technique is introduced. By using this proposed technique, LPF which does not produce the cutoff frequency error is designed. In order to compare the conventional design method and the new technique, two LPFs are designed by using both conventional and new method. Through the circuit simulations, 3D electromagnetic (EM) simulations, and measurements, the proposed new theory is validated.

In Chapter VI, a UWB bandpass filter with slotted ground structure introduced from [34] is studied for the purpose of extending the techniques of a slotted ground structure. Frequency responses over the different dimensions of parameters are also investigated. A coplanar waveguide UWB bandpass filter is designed and measured.

In Chapter VII, a rectenna is introduced as another application of the LPF with a dumbbell shaped slot (DSS). For good conversion efficiency from RF power to DC power, LPF used in rectenna must have low insertion loss. Rectenna also requires LPF with compact size to minimize its overall dimensions. LPF with a dumbbell shaped slot matches well with these requirements. The new rectenna is developed by utilizing the LPF with dumbbell shaped slot and tested. The measured conversion efficiency of this single unit rectenna is approximately equal to 80 %.

B. Recommendations and Further Research

A dumbbell shaped slot (DSS) in the ground plane has been extensively investigated and characterized through the theoretical and experimental work in this thesis. In analysis, a 3D EM simulation tool is used to estimate the capacitance and inductance from the DSS dimensions. Mathematical expressions of these capacitance and inductance over certain DSS dimensions and microstrip parameters need to be further studied. Other tuning techniques for a dumbbell shaped slot are also required to be operated as an active resonator or filter. These tuning abilities of DSS may be accomplished by using solid state devices or microfluidic techniques

REFERENCES

[1] J. D. Joannopoulos, R. D. Mead, and J. N. Winn, *Photonic Crystals*. Princeton, NJ: Princeton University Press, 1995.

[2] K. T. Chan, A. Chin, M.-F. Li, D.-L. Kwong, S.P. McAlister, D. S. Duh, W. J. Lin, and C. Y. Chang, "High-performance microwave coplanar bandpass and bandstop filters on Si substrates," *IEEE Trans*. *Microw*. *Theory Tech*., vol. 51, no. 9, pp. 2036-2040, Sep. 2003.

[3] D. Woo and T. Lee, "Suppression of harmonics in Wilkinson power divider using dual-band rejection by asymmetric DGS," *IEEE Trans*. *Microw*. *Theory Tech*., vol. 53, no. 6, pp. 2139-2144, June 2005.

[4] H. W. Liu, Z. F. Li, X. W. Sun, and J. F. Mao, "An improved 1D periodic defected ground structure for microstrip line," *IEEE Microw*. *Wireless Compon*. *Lett*., vol. 14, no. 4, pp. 180-182, April 2004.

[5] S.M. Han, C.-S. Kim, D. Ahn, and T. Itoh, "Phase shifter with high phase shifts using defected ground structures," *IEE Electronics Letters*, vol. 41, no. 4, pp. 196-197, Feb. 2005.

[6] J.-S. Lim, J.-S. Park, Y.-T. Lee, D. Ahn, and S. Nam, "Application of defected ground structure in reducing the size of amplifiers," *IEEE Microw*. *Wireless Compon*. *Lett*., vol. 12, no. 7, pp. 261-263, July 2002.

[7] M.-S. Jung, J.-S. Park, J.-B. Lim, and H.-G. Cho, "A novel defected ground structure and its application to a microwave oscillator," *33rd European Microwave Conf. Proc.,* Oct. 2003.

[8] C. Gao, Z. N. Chen, Y. Y. Wang, N. Yang, and X. M. Qing, "Study and suppression of ripples in passbands of series/parallel loaded EBG filters," *IEEE Trans. Microw. Theory Tech.*, vol. 54, no. 4, pp. 1519-1526, April 2006.

[9] T. Ming, Z. You-jun, Z. Sheng, and Z. Ling, "Novel high-Q band stop filter by using U-slot DGS," *Electronic Components and Materials*, vol. 26, no. 11, pp. 38-40, Nov. 2007.

[10] M. K. Mandal and S. Sanyal, "A novel defected ground structure for planar circuits," *IEEE Microw. Wireless Compon. Lett.*, vol. 16, no. 2, pp. 93-95, Feb. 2006.

[11] J. I. Park, C. S. Kim, J. S. Park, Y. Qian, D. Ahn, and T. Itoh, "Modeling of photonic bandgap and its application for the low-pass filter design," in *Asia-Pacific Microwave Conf., Dig.*, Dec. 1999, pp. 331-334.

[12] J. S. Lim, C. S. Kim, Y.T. Lee, D. Ahn, and S. Nam, "Design of lowpass filters using defected ground structure and compensated microstrip line," *Electron. Lett.*, vol. 38, no. 22, pp. 1357-1358, Oct. 2002.

[13] D. M. Pozar, *Microwave Engineering*, 3rd ed. Hoboken, NJ: John Wiley & Sons, Inc., 2005.

[14] G. L. Matthaei, L. Young, and E. M. T. Jones, *Microwave Filters*, *Impedance-Matching Networks*, *and Coupling Structures*. Dedham, MA: Artech House, Inc., 1980.

[15] H. J. Orchard, "Formula for ladder filters," *Wireless Eng*., vol. 30, pp. 3-5, Jan. 1953.

[16] R. E. Collin, *Foundations for Microwave Engineering*. New York, NY: McGraw-Hill, Inc., 1992.

[17] K. R. Demarest, *Engineering Electromagnetics*. Upper Saddle River, NJ: Prentice Hall, Inc., 1998.

[18] K. Chang, *Microwave Solid-State Circuits and Applications*. New York, NY: John Wiley & Sons, Inc., 1994.

[19] N. Yang and Z. N. Chen, "Microstrip line periodic structures with capacitive and resonant element loads," in *IEEE International Workshop on Antenna Technology*: *Small Antennas and Novel Metamaterials*, Mar. 2005, pp. 391-394.

[20] L. Brillouin, *Wave Propagation in Periodic Structures*, 2nd ed. New York, NY: Dover Publications, 1953.

[21] V. Radisic, Y. Qian, R. Coccioli, and T. Itoh, "Novel 2-D photonic bandgap structure for microstrip lines," *IEEE Microwave Guided Wave Lett*., vol.8, no. 2, pp.69-71, Feb. 1998.

[22] N. Yang, Z. N. Chen, Y. Y. Wang, and M. Y. W. Chia, "An elliptic low-pass filter with shorted cross-over and broadside-coupled microstrip lines," in *IEEE MTT-S Int*. *Mivrow*. *Symp*. *Dig*., June 2003, pp. 535-538.

[23] F. R. Yang, K. P. Ma, Y. Qian, and T. Itoh, "A uniplanar compact photonic-bandgap (UC-PBG) structure and its applications for microwave circuits," *IEEE Trans*. *Microw*. *Theory Tech*., vol. 47, no. 8, pp. 1509-1514, Aug. 1999.

[24] J. Liang and H.-Y. David Yang, "Radiation characteristics of a microstrip patch over an electromagnetic bandgap surface," *IEEE Trans*. *Antennas Propag*., vol. 55, no. 6, pp. 1691-1697, June 2007.

[25] C. T. Rodenbeck, M.-Y. Li, and K. Chang, "A novel millimeter-wave beam-steering technique using a dielectric-image line fed grating film," *IEEE Trans*. *Antennas Propag*., vol. 51, no. 9, pp. 2203-2209, Sep. 2003.

[26] R. S. Kshetrimayum and L. Zhu, "Guided-wave characteristics of waveguide based periodic structures loaded with various FSS strip layers," *IEEE Trans*. *Microw*. *Theory Tech*., vol. 53, no. 1, pp. 120-124, Jan. 2005.

[27] Ansoft, Designer© v3.0 and HFSS© v11.1, Pittsburgh, PA.

[28] D. Ahn, J. S. Park, C. S. Kim, J. Kim, Y. Qian, and T. Itoh, "A design of the low-pass filter using the novel microstrip defected ground structure," *IEEE Trans*. *Microw*. *Theory Tech*., vol. 49, no. 1, pp. 86-93, Jan. 2001.

[29] R. F. Harrington, *Time-Harmonic Electromagnetic Fields*. New York, NY: IEEE Press Series, John Wiley & Sons, Inc., 2001.

[30] K. Chang, *RF and Microwave Wireless Systems*. New York, NY: John Wiley & Sons, Inc., 2000.

[31] Federal Communications Commission, *Revision of Part 15 of the Commissions Rules Regarding Ultra-Wideband Transmission Systems*. First Report and Order, FCC 02. V.48, Apr. 2002.

[32] J.C. Liu, C.Y. Wu, M.H. Chiang, and D. Soong, "Improved dual-mode double-ring resonator with radial stub for UWB-filter design," *Microw*. *Opt*. *Technol*. *Lett*., vol. 44, no.3, pp.219-221, Feb. 2005.

[33] L. Zhu, H. Bu, and K. Wu, "Aperture compensation technique for innovative design of ultra-broadband microstrip bandpass filter," in *IEEE MTT-S Int*. *Mivrow*. *Symp*. *Dig*., June 2000, pp.315-318.

[34] L. Zhu and H. Wang, "Ultra-wideband bandpass filter on aperture-backed microstrip line," *Electronics Letters*, vol. 41, no. 18, pp.1015-1016, 2005.

[35] C. P. Wen, "Coplanar waveguide: A surface strip transmission line suitable for non-reciprocal gyromagnetic device application," *IEEE Trans*., *Microwave Theory Tech*., vol. 17, no. 12, pp. 1087-1090, Dec. 1969.

[36] I. Wolff, *Coplanar Microwave Integrated Circuits*. Hoboken, NJ: John Wiley & Sons, Inc., 2006.

[37] K.C. Gupta, R. Garg, and I.J. Bahl, *Microstrip Lines and Slot Lines*. Norwood, MA: Artech House, Inc., 1979.

[38] K. Chang, I. Bahl, and V. Nair, *RF and Microwave Circuit and Component Design for Wireless Systems*. Hoboken, NJ: John Wiley & Sons, Inc., 2002.

[39] R. H. George, "Solid state Power Rectifications," in E. C. Okress, Editor, *Microwave Power Engineering,* vol. 1, New York: Academic Press, 1968, pp. 275-294.

[40] J. O. McSpadden, L. Fan, and K. Chang, "Design and experiments of a high conversion-efficiency 5.8-GHz rectenna," *IEEE Trans*., *Microwave Theory and Tech*., vol. 46, no. 12, pp. 2053-2060, Dec. 1998.

[41] J. A. Hagerty, F. B. Helmbrecht, W. H. McCalpin, R. Zane, and Z. B. Popovic, "Recycling ambient microwave energy with broad-band rectenna arrays," *IEEE Trans*., *Microwave Theory and Tech*., vol. 52, no. 3, pp. 1014-1024, Mar. 2004.

[42] B. Strassner and K. Chang, "A circularly polarized rectifying antenna array for wireless microwave power transmission with over 78% efficiency," in *IEEE MTT-S Int*. *Microwave Symp*. *Dig*., June 2002, pp. 1535-1538.

[43] T.-W. Yoo and K. Chang, "Theoretical and experimental development of 10 and 35 GHz rectennas," *IEEE Trans., Microwave Theory and Tech*., vol. 40, no. 6, pp. 1259-1266, June 1992.

APPENDIX I

MAXIMALLY FLAT INSERTION LOSS PLOT

This section presents a matlab program for estimating the insertion loss pattern based on maximally flat type depending on the number of reactive elements. The matlab code is shown between the rows of asterisks. Figure 2 is plotted by this code.

```
**************************************************************************

x=[0:.01:5]; % Define the x-ranges

y1=10*log10(1+1*x.^2); % The maximally flat function for N=1
y2=10*log10(1+1*x.^4); %                 "               N=2
y3=10*log10(1+1*x.^6); %                 "               N=3
y4=10*log10(1+1*x.^8); %                 "               N=4
y5=10*log10(1+1*x.^10);%                 "               N=5

hold on
plot(x,y1);
plot(x,y2);
plot(x,y3);
plot(x,y4);
plot(x,y5);

hold off

**************************************************************************
```

APPENDIX II

BRILLOUIN DIAGRAM 1

This section presents a matlab program for estimating pass/stop bands of the periodic structure with a dumbbell shaped slot in the ground. The matlab code is shown between the rows of asterisks. Figure 21 is plotted by this code.

****

```
%  Brillouin diagram versus kd
%  DSS periodic structure
clear all;
clc;
Ldss=2.842*10^-9    % inductance of dumbbell shaped slot
Cdss=0.123*10^-12   % capacitance of dumbbell shaped slot
c=3*10^8            % speed of light
d=0.015             % distance between unit cell [in m]

%---------------------------------------------------------------------

resultkd=[];  % Generate matrix for 'kd' [in 'mm']
resultbd=[];  % Generate matrix for 'bd'(complex) [in 'radian']
resultAR=[];  % Generate matrix for 'AR'(real part of 'bd') [in 'radian']
resultad=[];  % Generate matrix for 'ad'(complex) [in 'Np']
resultAI=[];  % Generate matrix for 'AI'(imaginary part of 'ad')[in 'Np']

%---------------------------------------------------------------------

kd=0.00; % initial value of kd
for cl=0:1001   % loop
    kd=kd+0.01; % define k value

%---------------------------------------------------------------------

    x=(c*Ldss/d)*kd-(d/c*Cdss)./kd; % reactance: function of kd
    A=cos(kd)-(x./100).*sin(kd);                        % A
    B=j*((x./2).*cos(kd)+50*sin(kd)+x./2);              % B
    C=j*((x./5000).*cos(kd)+(1/50)*sin(kd)- x./5000);   % C
    D=cos(kd)-(x./100).*sin(kd);                        % D

%---------------------------------------------------------------------

    bd=acos((A+D)./2);  % Beta*d
% (Passband:real & Stopband:complex{all real values are the same})
    ad=acosh((A+D)./2); % Alpha*d
% (Passband:zero & Stopband:complex{all imaginary values are the same})
    AR=real(bd);        % Put real values in AR from bd.
```

```
    AI=imag(ad);        % Put real values in AI from ad.


%-------------------------------------------------------------------------

    resultkd=[resultkd;kd]; % Store 'kd'(0->10) in the resultkd matrix
% If "resultkd=[kd;resultkd], kd is save form 0 to 10 in the matrix
    resultbd=[resultbd;bd]; % Store 'bd' in the resultbd matrix
    resultAR=[resultAR;AR]; % Store 'AR' in the resultAR matrix
    resultad=[resultad;ad]; % Store 'ad' in the resultad matrix
    resultAI=[resultAI;AI]; % Store 'AI' in the resultad matrix
end
[resultkd,resultbd,resultad] % Shows data on screen
hold on
plot(resultbd,resultkd)
plot(resultad,resultkd, 'r')
hold off


**************************************************************************
```

APPENDIX III

BRILLOUIN DIAGRAM 2

This section presents a matlab program for estimating pass/stop bands of the periodic structure with a dumbbell shaped slot in the ground. The matlab code is shown between the rows of asterisks. Figure 22 is plotted by this code.

****

```
%  Brillouin diagram versus frequency
%  DSS periodic structure
clear all;
clc;
Ldss=2.842*10^-9    % inductance of dumbbell shaped slot
Cdss=0.123*10^-12   % capacitance of dumbbell shaped slot
c=3*10^8            % speed of light
d=0.015             % distance between unit cell [in m]

%---------------------------------------------------------------------

resultf=[];  % Generate matrix for 'f' [in 'hertz']
resultbd=[]; % Generate matrix for 'bd' [in 'radian']
resultad=[]; % Generate matrix for 'ad' [in 'Np']
resultAR=[]; % Generate matrix for 'AR'(real part of 'bd') [in 'radian']
resultAI=[]; % Generate matrix for 'AI'(imaginary part of 'ad')[in 'Np']

%---------------------------------------------------------------------

f=0.00;
s=10*10^6;
for cl=0:1200;  % loop
    f=f+s; % frequency sweep
    kd=(sqrt(1.9)*2*pi*d*f)./c;     % 'k' is the unloaded propagation constant
    x=(c*Ldss/d)*kd-(d/c*Cdss)./kd; % reactance: function of kd

%---------------------------------------------------------------------

    A=cos(kd)-(x./100).*sin(kd);                        % A
    B=j*((x./2).*cos(kd)+50*sin(kd)+x./2);              % B
    C=j*((x./5000).*cos(kd)+(1/50)*sin(kd)- x./5000);   % C
    D=cos(kd)-(x./100).*sin(kd);                        % D

%---------------------------------------------------------------------

    bd=acos((A+D)./2);  % Beta*d
    ad=acosh((A+D)./2); % Alpha*d
    AR=real(bd);        % Put real values in AR from bd.
```

```
    AI=imag(ad);        % Put real values in AI from ad.

%-----------------------------------------------------------------------

    resultf=[resultf;f];
    resultbd=[resultbd;bd];
    resultad=[resultad;ad];
    resultAR=[resultAR;AR]; % Store 'AR' in the resultAR matrix
    resultAI=[resultAI;AI]; % Store 'AI' in the resultad matrix
end

%-----------------------------------------------------------------------

[resultf,resultbd,resultad]
hold on
% If beta is pure real, alpha is pure imaginary [real(beta)=imag(alpha)].
% This is pass-band.
plot(resultf,resultbd)
% If alpha is pure real, beta is pure imaginary [real(alpha)=imag(beta)].
% if beta is complex number, alpha is also complex.
% Then, [real(beta)=imag(alpha), imag(beta)=real(alpha)]
% This is stop-band
plot(resultf,resultad,'r');
hold off
```

****

VITA

Dong Jin Jung was born in Asan, Korea. He received his B.S. degree in 2007 from Soonchunhyang University, South Korea. From 2005 to 2006, he was an undergraduate student member of the RF and Microwave Component Research Center (RAMREC) at Soonchunhyang University. In the fall semester of 2007, he started his M.S. study in the Electrical Engineering Department of Texas A&M University, Texas, USA. He is currently Vice President of Korean-American Scientists & Engineers Association at Texas A&M University. He also worked at the Engineering Laboratory of MIMIX BROADBAND, Houston, Texas as a student intern in the summer of 2008. His present research interest includes microwave and millimeter-wave devices and circuits, microwave integrated circuits, antennas, microwave power transmission, and electromagnetic scattering. Dong-Jin Jung's present address is 214 Zachry Engineering Center, College Station, TX 77843-3128. His email address is dongjin3558@tamu.edu.